https://doi.org/10.1016/j.combustflame.2016.08.010

Hypergolic Ignition by Head-on Collision of *N,N,N',N'*–tetramethylethylenediamine and White Fuming Nitric Acid Droplets

Dawei Zhang[1], Peng Zhang[1,*], Yueming Yuan[2], and Taichang Zhang[2]

1. Department of Mechanical Engineering, the Hong Kong Polytechnic University, Kowloon, Hong Kong

2. State Key Laboratory of High Temperature Gas Dynamics, Chinese Academy of Sciences, Beijing, 100190, People's Republic of China

* Corresponding author

E-mail address: pengzhang.zhang@polyu.edu.hk (P. Zhang)

Abstract

Hypergolic ignition by the head-on collision of a smaller N,N,N',N'−tetramethylethylenediamine (TMEDA) droplet and a larger white fuming nitric acid (WFNA) droplet was experimentally investigated by using a droplet collision experimental apparatus equipped with a time-resolved shadowgraph, a photodetector and an infrared detector. The investigation was focused on understanding the influence of droplet collision and mixing, which vary with the collisional Weber number (We = 20–220) and the droplet size ratio (Δ = 1.2–2.9) while have a fixed Ohnesorge number (Oh=2.5×10^{-3}), on the hypergolic ignitability and the ignition delay times. The hypergolic ignition was found to critically rely on the heat release from of the liquid-phase reaction of TMEDA and nitric acid, which is subsequent to and enhanced by the effective mixing of the droplets of proper size ratios. Consequently, the ignitability regime nomogram in the We-Δ space shows that the hypergolic ignition favors small Δs and large Wes; the ignition delay times tend to decrease with either decreasing Δ, or increasing We, or both. A non-monotonic variation of the ignition delay times with We was observed and attributed to the non-monotonic emergence of jet-like mixing patterns that enhance the droplet mixing and hence the liquid-phase reaction.

1. Introduction

1.1 Hypergolic Ignition

Spontaneous ignition of a hypergolic propellant occurs upon the contact with an oxidizer without external heat sources such as flames, sparks, hot gases and surfaces [1-4]. Using hypergolic propellants in rocket engines simplifies the engine design, allows the engine restart, and thereby increases the engine maneuverability. In a typical rocket engine combustor, the initially separated liquid fuel and oxidizer are brought together to react by the impingement of fuel and oxidizer jets. A lapse can be detected between the first contact of fuel and oxidizer and the occurrence of ignition, which is often characterized by rapid heat release and possibly concomitant visible light emission. Unlike the autoignition of a homogeneous mixture of non-hypergolic reactants, which can be defined characterized as by a "rapid" rise of temperature or pressure, the hypergolic ignition is inherently a physicochemical process involving mixing and reactions in both liquid and gas phases, and its definition is usually descriptive and system-dependent.

Many experimental methods have been developed for studying the ignition process of hypergolic propellants from different aspects and comprehensively summarized in a few reviews [2, 4]. Fletcher and Morrell indicated that the fundamental difference among these methods arises from the different modes of mixing [2]. The prevalent experimental methods are schematically shown in Figures 1(a)-1(d) in the order of approximately descending degree of premixing before reaction. Figure 1(a) schematizes the piston-driven apparatus, in which the reactants are rapidly mixed within a few milliseconds or less before being injected into a constant-volume reactor [5-8]. The observed ignition process is dominantly determined by chemical reactions and can be separated into three temporally sequential stages [2, 7, 8]: the first stage is the fast liquid-phase reactions yielding heat and gaseous species; the second stage is the relatively slow mixing and reactions in gas phase; and the third stage is the gas-phase ignition and combustion. Furthermore, the ignition delay is found to rely on the duration of the second stage, which is sensitive to the heat release from the liquid-phase reactions in the

first stage. Figure 1(b) schematizes the impinging jet test, in which the fuel and oxidizer are partially premixed before they are injected by the impinging nozzles into a confined chamber [9-11]. This apparatus can be used to simulate various temperature, pressure and concentration conditions met in rocket engine combustors. Figure 1(c) schematizes the widespread drop test for prescreening potential hypergolic propellants [12, 13]. In the test, a fuel drop is made to impact a small amount of oxidizer pool in either a glass cuvette or a flat tray. The fuel and oxidizer have minimal premixing before their liquid-phase reactions occur. Figure 1(d) schematizes the drop contact test, in which a suspended droplet of one propellant gradually approaches to an unrestrained pool of the other propellant [14-16]. Such a test was recently developed to resemble the hypergolic ignition initiated by droplet-droplet collisions with small impact inertia [14].

In spite of the worthy understanding in hypergolic ignition obtained with the experimental methods shown above, the influence of liquid-phase mixing in determining the ignition delay are either designedly eliminated from the rapid-mixing reactors, or partially suppressed in the impinging jet tests, or inseparably present in the drop tests. Moreover, it is difficult (if not impossible) to quantify the liquid-phase mixing in the drop tests because of the "wall effect" introduced by the cuvette walls, or the quartz rod or filament for suspending the droplet, or the surface supporting the unstrained liquid pool. In view of that the impinging jets of hypergolic propellants are atomized into droplets in rocket engine combustors, and that the frequent collisions of propellant droplets tend to promote the liquid-phase fuel-oxidizer mixing and therefore the ignition, an experimental method-free from any wall effect as shown in Figure 1(e)-for studying the hypergolic ignition initiated by the binary collision of droplets, as shown in Figure 1(e), is desirable but has not been attempted.

Recent interests in gelled hypergolic propellants (GHP) [17-19] further signify the study of hypergolic ignition by droplet collision. Because of the reduced vapor pressure of propellants by gelling, the ignition of GHPs can be only triggered in liquid phase after a succession of fluid-dynamical processes: the collision, the coalescence and the mixing of the

fuel and oxidizer droplets. It is nevertheless known that a collision of two liquid droplets unnecessarily results in a coalescence, which in turn cannot warrant a sufficient and rapid mixing within the coalesced droplet. Consequently, it is worthwhile to briefly summarize the current understanding in droplet collision dynamics, especially those pertinent to the droplet internal mixing, in the following subsection.

1.2 Collision Dynamics and Internal Mixing of Droplets

Being of importance in understanding many industrial and natural processes, binary droplet collision in a gaseous medium has been a subject of considerable interest for decades [20, 21]. The majority of earlier experiment research was focused on identifying various collision outcomes of two identical droplets and on their variation with the controlling parameters: the collision Weber number, *We*, measuring the relative importance of droplet inertia compared with its surface tension, and the impact parameter, *B*, characterizing the deviation of droplet trajectories from the head-on condition. For water, alkanes and alcohols, five distinct collision outcomes are effected by varying *We* and *B*: (I) coalescence after minor deformation, (II) bouncing, (III) coalescence after substantial deformation, (IV) coalescence followed by separation for near head-on collision (a.k.a. reflective separation with small *B*), and (V) coalescence followed by off-center collision (a.k.a. stretching separation with large *B*). Droplet splattering occurs at the higher *We*s, often over a thousand, which are infrequently encountered in real engine conditions [22].

Theoretical efforts have been made to understand the experimental observations. Zhang and Law [5] developed a comprehensive theory to explain the nonmonotonic transitions from Regime (I) to (II) and from (II) to (III). The theory reveals that the occurrence of droplet coalescence or bouncing depends on whether or not the clearance between the impacting interfaces can reach the critical range (typically tens of nanometers) of the van der Waals force before the droplets have totally lost the translational kinetic energy of their relative motion. Several contributing physical factors, such as the rarefied nature of the intervening

gas flow between the droplets, the viscous dissipation of the droplet internal motion, and the van der Waals force between the droplet interfaces, were identified and incorporated into the theory. Various models have also been proposed to explain the transition between Regime (III) to (IV) [3,6–8] and the formation of satellite droplets for Regime (V) [9–10]. The viscous dissipation through the internal motion of merged droplet was found to suppress the droplet separation and therefore stabilize the droplet.

The ambient pressure influences the collision outcomes [20, 23]. Specifically, droplets tend to bounce back with increasing the ambient pressure because the increased inertia of the gas film separating the droplets becomes more resistant to be drained out to effect the interface merging [24]. By the same token, droplets tend to coalesce with decreasing the ambient pressure. For instance, bouncing is absent for water droplets at atmospheric pressure but present at reduced pressures; coalescence is present for n-tetradecane droplets at atmospheric pressure but absent at elevated pressures.

The size ratio, Δ, usually defined by the ratio of the diameter of the bigger droplet to that of the smaller one, affects substantially the collision outcomes. Previous studies [25-27] have demonstrated that droplet separation is suppressed and hence droplet coalescence is promoted by increasing the size ratio. It is known that droplet separation occurs, at relatively high Weber numbers, when the surface tension of the temporarily coalesced droplet cannot hold the excess kinetic energy of the collision. Increasing the size ratio tends to increase the viscous dissipation within the coalesced droplet, which stabilizes the droplet by dissipating the excess energy.

The effects of liquid viscosity on the collision outcomes, particularly on suppressing the droplet separation through the viscous dissipation, were observed by Jiang et al. [28] and Qian and Law [23], and further confirmed and characterized in subsequent studies [29-31]. The Volume-of-Fluid simulation of Dai and Schmidt [29] on the head-on collision of equal-size droplets shows that the dependence of the dissipated energy and the maximum deformation on the collision Reynolds number decreases with increasing the Reynolds number up to 200.

Their results suggest that the viscosity effect on the maximum deformation becomes insignificant at sufficiently high Reynolds number. The experiments of Gotaas et al. [30] on the collision of equal-size droplets of wide ranges of viscosity from 0.9×10^{-3} kg/(m·s) to 48×10^{-3} kg/(m·s) and the Weber number from 10 to 420 show that the transition Weber number for the droplet separation linearly increases with the Ohnesorge number (Oh) for the droplets with Oh<0.04 and exponentially increases with the Oh for the highly viscous droplets with Oh>0.04.

Another important aspect of droplet coalescence is the subsequent internal mixing, which has gained increasing attentions in recent years for its relevance in the microfluidics and hypergolic propellant systems involving liquid-phase reactions [32-38]. An important understanding gained from the recent studies is that the internal mixing is minimal for the head-on collision of two identical droplets due to the intrinsic symmetry across the collision plane. Effective mixing requires breaking the symmetry by introducing differences between the droplets to either surface tensions, or viscosities, or diameters. Tang et al. [37] investigated experimentally and numerically the internal mixing of unequal-size droplets and identified the jet-like mixing patterns varying with *We* and Δ, as shown in Figure 2. For droplets with a relatively small viscosity (for example, water and n-decane), the internal mixing in the coalesced droplet is facilitated by the emergence of jet-like patterns at small and large Weber numbers, and however such jet-like mixing patterns do not develop at intermediate Weber numbers. Mechanically, the jet formation at small *We*s is driven by the capillary pressure difference of the droplets; it is suppressed by the substantial droplet deformation at intermediate *We*s; it reemerges at large *We*s due to the droplet stretching in the direction of the large impact inertia. In addition, the jet-like mixing is enhanced by increasing the size ratio because it favors the concentrated impact inertia of the smaller droplet. The jet-like mixing is suppressed for liquids with large viscosities (for example, n-tetradecane) that reduce the impact energy through viscous dissipation.

Several inferences of the above understanding on droplet coalescence and mixing can be drawn for hypergolic ignition by droplet collision. First, hypergolic ignition may favor relatively low ambient pressures because droplet coalescence is the prerequisite for the subsequent droplet mixing but it is suppressed at elevated pressures. Second, hypergolic ignition may favor a large size disparity for enhanced droplet coalescence and mixing. Third, hypergolic ignition may vary significantly with *We* because the degree of droplet mixing depends on *We* non-monotonically through the jet-like mixing patterns. It is also noted that these inferences may be reformed when droplet collision and mixing are coupled with chemical reactions.

1.3 Hypergolic Ignition of TMEDA and WFNA

Tertiary amine *N,N,N',N'*–tetramethylethylenediamine [$(CH_3)_2NCH_2CH_2N(CH_3)_2$, referred to as TMEDA hereinafter] has been tested as an alternative, 'green' hypergolic propellant for future rocket and missile engines to replace the acutely toxic and potentially carcinogenic hydrazine and its derivatives. Compared with the widely-used monomethylhydrazine (CH_3NHNH_2, referred to as MMH hereinafter), TMEDA remains as a liquid in a wider range of temperatures and is 8.4 times less toxic based on the LD_{50} data, and therefore reduces the threat of its vapor exposure to the personnel and environment during its storage and handling. Furthermore, when used with nitric acids (NA) as the oxidizer, such as red fuming nitric acid (RFNA) and white fuming nitric acid (WFNA), TMEDA has comparable specific impulses, density impulses and ignition delays, making TMEDA an attractive MMH substitute.

Compared with the extensively studied MMH and other amines, the TMEDA/NA system was recently investigated in only a few theoretical and experimental studies. McQuaid et al. [39, 40] performed the ab initio quantum chemistry and molecular dynamics studies of various multi-amines and correlated the advantageous hypergolicity of TMEDA to the orientation of its amino lone pair electrons. The density functional theory (DFT) study of Liu et al. [41]

identifies two key reactions affecting the ignition delay of TMEDA/NA: the exothermic proton transfer reaction from NA to TMEDA to form the dinitrate salt, TMEDADN, in liquid phase,

$$\mathrm{TMEDA} + 2\mathrm{HNO_3} \rightarrow \mathrm{TMEDADN}, \quad (1)$$

and the subsequent gas-phase reactions between TMEDA and NO_2, the major product from the thermal decomposition of NA. The important role of the exothermicity of liquid-phase reactions in determining the hypergolic ignition delay was also confirmed by Zhang et al. [42], whose DFT study employs eight different theoretical methods to compare the TMEDA/NA system with that of 2–azido–*N,N*–dimethylethanamine (DMAZ) and NA.

Dambach et al. [16] conducted drop contact tests and drop tests to study the hypergolic ignition of TMEDA/RFNA. Ignition was observed for all the drop tests but not for the drop contact tests, implying that the droplet impact promotes the ignition by enhancing the mixing. Their drop contact tests also show that ignition does not occur when the volume ratios of TMEDA to RFNA are small.

Wang et al. [11, 13] used a confined interaction setup resembling the jet impinging apparatus and a drop test to study the hypergolic ignition of TMEDA with an NA of 90% purity. Their Fourier transform infrared spectrometry measurement of species confirms the existence of TMEDADN, which appears as a solid particulate cloud. The exothermic salt formation reaction was found crucial for the heat needed for evaporating the reactants, decomposing NA to NO_2, and the subsequent reactions of TMEDA and NO_2.

The present experimental study attempts to study the hypergolic ignition by the binary, head-on collision of a smaller TMEDA droplet and a larger WFNA droplet in atmospheric air, with the emphasis on the influence of the collision parameters, such as We and Δ, on the ignition delays. Only head-on collisions (B=0) are considered in the study to avoid the additional complexity of off-center collisions ($B\neq0$), which merit future studies. Because unequal-size droplet collisions promote droplet coalescence and mixing, the size ratio is

another crucial variable besides the Weber number. Furthermore, WFNA is used to minimize the intervention of other components contained in RFNA or in other NAs. We shall present the study as follows. The experimental apparatus and the measurement methods are expatiated in Section 2. The results for a representative case are presented in Section 3 to illustrate the hypergolic ignition processes. A *We*-Δ regime nomogram for the hypergolic ignitability is also presented in the section. The influences of *We* and Δ on the ignition delays are discussed in Sections 4 and 5, respectively, followed by concluding remarks, in Section 6.

2. Experimental Apparatus and Measurement Methodology

2.1 Droplet Collision Apparatus

The schematic of the droplet collision apparatus established for the present study is shown in Figure 3. Droplets are generated by two independent droplet nozzles, (1) for WFNA and (2) for TMEDA, and collected by a tray (3). The nozzles are connected to the pressurized liquid tanks (4) and the pressure of pure nitrogen from the gas tank (5) is regulated by two SMC pressure reducing valves (6) with an accuracy of 0.1kPa and are powered by a 24V direct current (7).

The key component of the TMEDA droplet generator is an electromagnetically controlled micro valve, SMLD 300G, made by Fritz Gyger AG. The valve has a typical response time of 400μs, a maximum dispensing frequency of 3000Hz, and a repeat accuracy of higher than 95%. The droplet generator is mounted on a micrometric *XYZ* stage (8) to precisely adjust the positions and angles of the dispensing TMEDA droplets. The droplet generator is triggered by a function generator with tunable time delays, so the droplet can be spatially and temporally regulated to collide with the WFNA droplet generated separately. The sizes of the TMEDA droplets vary from 0.5mm to 1.2mm in the present study and are mainly determined by the orifice diameter of the valve nozzle. The switch-on duration of the nozzle, which is controlled by the pulse generator (9) through a controlling circus (10), moderately affects the droplet size.

The dispensing velocity of the TMEDA droplets can be changed with the nitrogen gas pressure through the pressure reducing valve (6).

Because WFNA is strongly corrosive to the SMLD 300G valve and other commercial droplet generators, a simple but functional droplet generation nozzle was designed and manufactured for the present study. The needle-shape nozzle with a diameter of 0.2mm is made of Teflon (Polytetrafluoroethylene) and mounted downwardly to generate WFNA droplets of 1.45 mm with a frequency of 2-3 Hz by the pressurized nitrogen gas. Once a WFNA droplet is collided by a TMEDA droplet, their motion will substantially deviate from the trajectories of the other WFNA and TMEDA droplets. As a result, the droplet collision and subsequent ignition processes are not intervened by other droplets generated from the nozzles.

2.2 Measurement Methodology

The experimental setup for the shadowgraph imaging, photoelectric and infrared detections is shown in Figure 4. The temporally resolved shadowgraph images are recorded by a Phantom V711 camera (1), with an imaging speed of 5000 frames per second. Each image consists of 1024 × 800 pixels and one pixel represents a physical two-dimensional grid of 20μm × 20μm. With the enlarging optical lenses, the camera is able to capture an about 4cm × 3cm region (one pixel represents 40μm×40μm), which is sufficiently large for observing the entire collision and ignition processes. A light-emitting diode (2) is placed oppositely to the high-speed camera as a back light source.

Because the hypergolic ignition of TMEDA/WFNA is accompanied with luminous flames and a large amount of heat release [11, 13], visible and infrared radiations are measured to detect the occurrence of the ignition. The THORLABS DET10A photodetector (3) has a wavelength range of 200nm ~ 1100nm and a rise time of 1ns. The liquid-nitrogen-cooled infrared detector (4) of Infrared Associates, Inc. has a wavelength of 2μm ~ 5μm and a response time of 1μs. It will be seen shortly that these two measurements with high

responsivities provide validations to the ignition delay time determined by analyzing the time-resolved shadowgraph images.

The photodetector and the infrared detector are placed at the same horizontal level as that of the high-speed camera. The convex lens for visible lights (5) and the one with infrared antireflection coatings (6) are 2 inches in diameter. Synchronized with the high-speed camera and externally triggered by a pulse generator (8), the oscilloscope (7) collects and displaces the voltage signals from the visible light photodetector and the infrared radiation detector.

The diameters, the relative velocity and the collision impact parameter of the TMEDA and WFNA droplets are measured from the shadowgraph images, as shown in Figure 5. The grayscale images of the shadow photographs are stored with a resolution of 8 bits per sample pixel, which results in 256 different grayscale levels for the shade of gray. The lowest level, 0, denotes the darkest and the highest level, 256, the brightest. With the average grayscale level set to be 100, the grayscale levels are lower than 5 in the region occupied by droplets and the opaque gaseous species, and are higher than 250 in the region occupied by luminous flames. The small, bright spots in the centers of the droplets are due to the light reflection.

Because of the large difference of grayscale levels in the shadowgraph images, we can use the MATLAB software to count the grayscale level for each pixel, compute the local gradient of grayscale levels and identify the outmost edge of the droplet surface, where the largest gradients are obtained. Consequently, the droplet shape can be determined with an accuracy of one pixel and the measured droplet diameters have errors less than 7%, as the smallest droplet occupies about 15 pixels. The droplet velocity can be determined, within an error of 3%–8%, by locating the droplet center in five successive images within 1.0 ms, and subsequently calculating and averaging the time derivatives of the coordinates of the droplet center. The impact parameter is defined by $B = x/L$, in which x is the projection of the separation distance L between the droplet centers in the direction normal to the relative velocity and can be determined after the velocities of the two droplets are obtained. In the

present study, the impact parameter is controlled to be smaller than 0.1 to minimize the influence of off-center collisions.

3. Ignition Phenomena, Ignition Delay Time and Ignitability

3.1 Descriptions of Ignition Phenomena

The phenomena of the hypergolic ignition by the collision of a smaller TMEDA droplet and a larger WFNA droplet are described by using a representative case of $We = 60.9$ and $\Delta = 1.6$. Choosing WFNA as the excess propellant is suggested by the stoichiometry of the exothermic liquid-phase reaction (1) and have been used in previous drop tests [11, 13]. The Weber number is defined by $We = \rho_O D_O U^2/\sigma_O$ and the size ratio by $\Delta = D_O/D_F$, where ρ, σ, and D are the density, the surface tension and the diameter of the droplets; U is the relative velocity between the droplets; the subscript "O" denotes WFNA and "F" TMEDA. These nondimensional numbers are based on the physical properties of the WFNA droplet because D_O is fixed at 1.45mm in the present experiment.

Dimension analysis shows that the collision of two unlike, miscible droplets relies on not only We and Δ but also the Ohnesorge number, $Oh = \mu_O/\sqrt{\rho_O \sigma_O D_O}$; the density ratio, ρ_O/ρ_F; the viscosity ratio, μ_O/μ_F; the surface tension ratio, σ_O/σ_F; the gas-liquid density ratio, ρ_g/ρ_O; and the gas-liquid viscosity ratio, μ_g/μ_O. The fluid-dynamic effect of liquid viscosity, particularly on suppressing the droplet separation through the viscous dissipation of the droplet internal motion, can be characterized by either the Ohnesorge number or the Reynolds number, $Re = \rho_O D_O U/\mu_O$, but not both at the same time because they are interdependent by $Re = \sqrt{We}/Oh$ when We is given.

As the physical properties of the two propellants, the ambient gas, and D_O are fixed in the present experiment, only We and Δ can be independently varied by changing the impact velocity and the size of the TMEDA droplet; the Ohnesorge number, $Oh = 2.5 \times 10^{-3}$, is fixed in the present study; $Re = \sqrt{We}/Oh$ varies accordingly with We; the other ratios are fixed as constant parameters.

For a unified description, we have introduced and presented the nondimensional time $T = t/t_{\text{osc}}$ where $t_{\text{osc}} = \sqrt{\rho_o R_o^3/\sigma_o}$is approximately the natural oscillation time of the WFNA droplet and is fixed at $3.3ms$ in the present study. Considering the present problem is not a purely surface-tension-driven flow and the droplet impact inertia play an important role, we have also presented another characteristic time defined by $\text{t}_{\text{inertia}} = D_o/U = 9.3ms/\sqrt{We}$ for comparison. It is noted that physical times in lieu of the nondimensional times will be referred to throughout the below discussion.

The shadowgraph images at selected times are shown in Figure 6, where $t = 0$ is defined as the moment when the droplets are about to collide. An axisymmetric coordinate system is established on the WFNA droplet so that the head-on collision is along the z-direction. It is noted that different reference lengths are used for a clear presentation of the entire process, which spatially expands from a few hundred microns to a couple of centimeters. Resembling the drop tests of TMEDA/NA by Wang et al. [11, 13], the observed phenomena can be visually divided into five stages as follows.

Stage I (0ms – about 4.0ms): droplet coalescence and deformation. The dominant phenomena in this stage are droplet collision, coalescence and deformation, which are similar to those observed in the collision of two nonreactive droplets [25, 37]. A slightly dark "tail" behind the WFNA droplet is the shadow of NA vapor, which is negligible during this stage because of the relatively low droplet temperature and the short time. The droplet surface becomes increasingly blurry after about 2.0ms because the exothermic TMEDA/NA liquid-phase reaction starts increasing the droplet temperature and thereby expediting the droplet vaporization.

Stage II (about 4.0ms – about 20.0ms): droplet heating and vaporization. This stage is characterized by the spread of the blurred droplet surface, which is quickly concealed by the expansion of the opaque vapors and gaseous species. We can infer that droplet is being heated up from the inside to the surface, because the exothermic liquid-phase reaction occurs with the merged droplet where the effective mixing of TMEDA and WFNA can be achieved by

forming the jet-like flow patterns, as discussed in Introduction. This inference is consolidated by the vortex ring formation observed in Wang et al.'s drop tests [11, 13], which is a well-known counterpart of the jet formation in the drop-pool interaction. Because of the droplet heating, the surface temperature has not been fully increased in this stage and there by droplet vaporization is slower than that in the subsequent stage.

Stage III (about 20.0ms – about 30.0ms): rapid vaporization and reactions. The droplet vaporization and the reactions in both liquid and gas phases become significantly faster because of the increased droplet temperature. It is seen that, a large amount of vapors and gaseous species are produced; they appear as a large opaque area in the images.

Stage IV (about 30.0ms – about 31.0ms): ignition in gas phase. The ignition occurs at 30.6ms as the emergence of a bright kernel within the opaque area, implying the over-exposed luminous flame. The temporally resolved images enable the visual determination of the ignition delay time to be between 30.2ms and 30.8ms. Meanwhile, the shape and area of the opaque region do not have significant changes, but the grayscale levels of the ignition kernel vary substantially.

Stage V (after about 31.0ms): flame propagation and combustion. The luminous flame outwardly propagates in the gaseous species, as the opaque region recedes while the bright region expands within 4–5ms. When the opaque gaseous species are consumed exhaustively, the flame extinguishes and a nonflammable condensed-phase product is left behind, as clearly seen in Figure 7 for its solid-like surface appearance. It is also seen that, the volume of the product does not significantly change from 32.4ms to 44.0ms, and therefore substantiates its non-flammability.

3.2 Determination of Ignition Delay Time

As discussed in Introduction, the definition of hypergolic ignition is usually descriptive and system-dependent. For example, the hypergolic ignition in the common drop-test is defined as either the appearance of a flame as an indicator of reactivity [41] or the

emergence of a visible luminous kernel in the gas phase above the liquid surface [11]. In the drop contact test of Dambach et al., the hypergolic ignition is defined as a highly transient phenomenon, which produces a flame after a multitude of complex coupled physical and chemical processes have occurred [14]. To accurately determine the ignition delay time in the present experiment, a method based on analyzing the grayscale levels of the shadowgraph images is used in the present study. As has been discussed in Section 2, the average grayscale level of the background in each shadowgraph image is set to be 100; the dark areas representing either the droplets or the opaque gaseous species have the grayscale levels below a lower threshold value such as $G_{low} = 5$; the bright areas representing the luminous flames have grayscale levels above a higher threshold value such as $G_{high} = 250$. Consequently, two time-dependent ratios can be defined by

$$r_d = N_d(t|G < G_{low})/N, \quad r_b = N_b\big(t|G > G_{high}\big)/N \tag{2}$$

$N_d(t|G < G_{low})$ and $N_d\big(t|G > G_{high}\big)$ are the total numbers of pixels having the grayscale levels, G, lower than G_{low} and higher than G_{high}, respectively; N is the total number of pixels in the image.

Figure 8(a) shows the procedure of the grayscale level analysis. The monotonic rise of r_d from 0ms to about 30ms indicates the increased amount of opaque gaseous species from the droplet vaporization and the gas-phase reactions. Meanwhile, r_b remains a negligibly small value because ignition has not occurred. Stages I-III identified in Section 3.1 are manifest in this figure: r_d remains constant during Stage I (0ms–4ms), implying little liquid vaporization; Stage II (4ms–22ms) is characterized an approximately linear increase of r_d; Stage III (22ms–30ms) shows another approximately linear increase of r_d with a larger slope, implying the faster droplet vaporization after the completion of droplet heating.

During Stage IV (30ms–35ms), r_d decreases rapidly due to the consumption of the opaque gaseous species; r_b increases simultaneously because of the emergence and expansion of the luminous flames. The ignition delay time (abbreviated as IDT hereinafter) can be

unambiguously defined as the instant corresponding to the turning point of r_d and r_b, namely, 30.6ms with an uncertainty of less than 0.2ms. Stage V starts at 35.6ms when r_b reaches its peak value, as a result of the full expansion of the luminous flames. This stage ends at around 44.0ms, when the luminous flames disappear. The value of r_d at 44.0ms is slightly larger than that at the initial time because of the opaque unburned gases and the condensed-phase products.

To quantify the sensitivity of the IDT to the arbitrarily chosen threshold values in Equation (2), we repeated the above analysis by using another two combinations of G_{low} and G_{high} and compared the results in Figure 8(b). It is seen that the turn points of r_d and r_b remain almost unchanged to the different threshold values and the uncertainty is less than 0.1ms. For consistency, $G_{low} = 5$ and $G_{high} = 250$ were used in the present study for determining all the IDTs.

To further validate the grayscale level analysis of shadowgraph images, we measured visible lights and the infrared radiation, as shown in Figure 9(a). During the first three stages, the two voltage signals denoting the intensities of the visible lights and the infrared radiations remain constants regardless of the fluctuations due to the background noise. The occurrence of ignition is indicated by the simultaneous increases of both signals at 30.6ms, as shown clearly in Figure 9(b), which is identical with the result from the grayscale analysis. It is also seen that the intensity signal of the visible lights increases to the peak value at about 35ms and subsequently decreases to its initial value after 40ms. Although the intensity signal of the infrared radiation increases almost synchronously with that of the visible lights, it gradually decreases after 40ms, because the gas temperature slowly decrease due to the heat loss to the environment.

3.3 Regime Nomogram of Ignitability

A large number of experiments on the hypergolic ignitability by droplet collision have been conducted and the results are presented as a regime nomogram in the *We-Δ* parameter

space, as shown in Figure 10. An approximately straight line, fitted as $\Delta_{cr} = 0.0044We + 1.82$, separates the *We*-$\Delta$ subspace of *We* = 20–220 and Δ = 1.2–2.9 into two regimes: the ignitable regime below the line and the non-ignitable regime above it. It is seen that increasing the size ratio suppresses the ignition and therefore a larger Weber number is required to promote ignition. In the regime nomogram, the variation of *We* not only affects the internal mixing within the coalesced droplet but also causes the droplet separation, which may drastically change the subsequent chemical reactions in both liquid and gas phases. The detailed discussions on the effects of *We* and Δ will be presented in the following sections.

4. Weber Number Effects on Ignition Delay

In order to illustrate the effects of the Weber number, *We*, on the IDT, the temporally resolved shadowgraphs for four cases are shown in Figure 11(a)–(d). Only sixteen images at selected times are presented for each case for simplicity and clarity: the first four images for Stage I, the second four for Stage II, the third four for Stage III and the last four for Stages IV and V. The four cases have the same size ratio, Δ = 1.6, as that of the representative case discussed in Section 3, but two have the smaller *We* = 37.0 and *We* = 52.0, compared with *We* = 60.9 of the representative case, and the other two have the larger *We* = 70.8 and *We* = 83.0.

Compared with the representative case, the case with *We* = 37.0 has a longer Stage II as seen in Figure 11(a), which implies a slower droplet heating process as the result of a probably less degree of droplet mixing at the smaller impact inertia. Meanwhile, the prolonged droplet heating process may result in more heat loss to the environment, which in turn results in a prolonged Stage III and a postponed ignition. The IDT of this case is 41.6ms.

As the *We* increases to 52.0, one may expect to observe an IDT between 30.6ms (at *We* = 60.9) and 41.6ms (at *We* = 37.0). Surprisingly, a substantially smaller IDT of 29.2ms was observed and mainly attributable to the significantly expedited droplet vaporization, as clearly seen in Figure 11(b). A possible explanation to the observation is the non-monotonic emergence of the jet-like mixing patterns with varying the Weber number, as discussed in

Introduction. The decrease of the IDT from 41.6ms at *We* = 37.0 to 29.2ms at *We* = 52.0 can be attributed to the mixing enhancement by increasing the Weber number. The increase of the IDT to 30.6ms at *We* = 60.9 may be caused by the suppression or disappearance of the jet-like mixing pattern. This speculation is further consolidated by the case with *We* = 70.8, in which a longer IDT of 31.2ms is seen in Figure 11(c). A direct visualization of the droplet mixing is however not available in the present study but merits future study.

Further increasing the Weber numbers can effect the decrease of IDT as the result of either the re-emergence of the jet-like mixing pattern, or the substantially increased droplet deformation, or both. The jet formation promotes the droplet internal mixing and the liquid-phase reaction; the droplet deformation augments the droplet surface area and hence the vaporization rate. As shown in Figure 11(d) for the case with We = 83.0, the coalesced droplet substantially stretches along the direction of collision and results in a disk-shape deformation at 9.0ms. The significantly deformed droplet provides a larger surface area for the vaporization, as showed by a large amount of opaque gaseous species at 18.0ms. Although the droplet separation eventually occurs, as clearly seen at the times after 24ms, a shorter IDT of 26.0ms is obtained in comparison with those of smaller Weber numbers. The two separated condensed-phase products are the proof of the droplet separation.

The dependence of the IDTs on the Weber numbers at the various size ratios of 1.3, 1.6 and 2.2 are shown in Figure 12. Several observations can be made from the results. First, the IDT has an overall tendency of decreasing with increasing *We* because of the enhanced droplet deformation and mixing, both of which expedite the droplet vaporization and hence the subsequent gas-phase ignition. Second, the subtle, non-monotonic variation of the IDT with *We* can be found at all the size ratios, probably attributed to the non-monotonic emergence of jet-like mixing pattern. Third, as the *We* increases to be sufficiently high, the IDTs are as small as 15ms and do not show significant changes with *We*. This substantiates that the IDT at high *We*s will be independent of mixing but controlled by the chemical reactions of the propellants [2]. Fourth, in the case of Δ = 2.2, no ignition was observed for the

*We*s smaller than 60.9. In addition, the IDTs tend to increase with the size ratios: the curve presenting for Δ = 2.2 is above that for Δ = 1.6, which in turn is above that for Δ = 1.3. These results imply that the size ratio plays a vital role in the ignition process, which will be discussed in the next section.

5. Size Ratio Effects on Ignition Delay

In order to illustrate the effects of the droplet size ratio, Δ, on the IDTs, the temporally resolved shadowgraphs for three cases are shown in Figure 10. The three cases have the same Weber number, 60.9, as that of the representative case discussed in Section 3, but one has a smaller Δ = 1.2 and the other two have larger Δ = 2.2 and Δ = 2.8.

Compared with the representative case with Δ = 1.6, the case with Δ = 1.2 exhibits similar droplet collision and ignition processes, as seen in Figure 13(a). Nevertheless, the shorter ignition delay time of 25.2ms seems to contradict with the argument that increasing the size ratio enhances the droplet mixing and therefore expedites the ignition. This contradiction can be resolved by considering the chemical stoichiometry of the liquid-phase reaction (1). The overall equivalence ratio [43, 44] for the TMEDA/NA liquid-phase reaction can be defined as

$$\Phi_{\text{overall}} = \frac{M_{\text{TMEDA}}/M_{\text{NA}}}{(M_{\text{TMEDA}}/M_{\text{NA}})_{st}} = \frac{\tilde{V}_{\text{NA}}}{\tilde{V}_{\text{TMEDA}}}\frac{2}{\Delta^3} \approx \frac{0.56}{\Delta^3} \quad (3)$$

Where $\tilde{V}_{\text{NA}} = 41.65$ cm^3/mol and $\tilde{V}_{\text{TMEDA}} = 149.66$ cm^3/mol are the molar volumes. It is noted that the reaction does not occur at Φ_{overall} in the present non-premixed system, that Φ_{overall} has an indirect effect on the reaction, and that Φ_{overall} can be used as an indicator for the amount of maximally possible reaction heat release.

Using Equation (3), we can have $\Phi_{\text{overall}} = 0.32$ for Δ = 1.2, and $\Phi_{\text{overall}} = 0.15$ for Δ = 1.6. The larger Φ_{overall} in the case with Δ = 1.2 may result in a larger amount of heat release, which has been proven to be critical to the subsequent fuel vaporization and decomposition. In addition, we can infer that, although the ignition favors the enhanced mixing by increasing the

sizer ratio, it is more sensitive to the overall equivalence ratio, which decreases cubically with the size ratio. This inference is confirmed by the two cases of Δ = 2.2 and 2.8, in which no ignition happens as shown in Figure 13(b)-(c). The possible reason for the non-ignitability of these two cases is that their overall equivalence ratios ($\Phi_{\text{overall}} = 0.05$ and $\Phi_{\text{overall}} = 0.025$) are too small for the liquid-phase reaction to generate enough heat for fuel vaporization. The deficient vaporization is manifestly seen in the shadowgraph images.

Figure 14 shows the dependence of the ignition delay times on the size ratio at We = 60.9 and We = 83.0. With regard to the liquid-phase reaction between WFNA and TMEDA, the unity overall equivalence ratio corresponds to Δ = 0.8. Therefore, all the cases shown in the figure can be considered "fuel lean" and the ignition tends to increase monotonically with increasing Δ and hence decreasing Φ_{overall}. A plateau of the IDTs can be observed for Δ = 1.33~1.55 at *We* = 60.9, and for Δ = 1.4~1.55 at *We* = 83.0. This may be caused by the competition between the liquid-phase reaction, favoring small Δs, and the droplet mixing, favoring large Δs. As the overall equivalence ratio cubically decreases with Δ, the liquid-phase reaction dominates over the mixing enhancement in determining the IDT.

6. Concluding Remarks

Hypergolic ignition by a smaller TMEDA droplet colliding head-on with a larger WFNA droplet was experimentally studied for its relevance to rocket propulsion with hypergolic propellants. The newly established experimental apparatus eliminates the wall effect existing in the standard drop tests and enables to mimic the hypergolic ignition by the collision of two freely moving droplets. The present study was focused on understanding the influence of the droplet collision and mixing, which vary with the Weber number (*We*) and the size ratio (Δ) while at a fixed Oh=2.5×10^{-3}, on the hypergolic ignitability and the ignition delay times. The hypergolic ignition processes were visually captured by time-resolved shadowgraph. The ignition delay times were determined, with an uncertainty of less than 0.2ms, by the grayscale

level analysis of the shadowgraph images, which has been validated by the photoelectric methods based on visible lights and infrared radiations.

The hypergolic ignitability of TMEDA/WFNA can be characterized by a regime nomogram in the We-Δ parameter subspace of We = 20–220 and Δ = 1.2–2.9. An approximately linear line fitted as $\Delta_{cr} = 0.0044We + 1.82$ divides the subspace to the "ignitable" regime below Δ_{cr} and the "non-ignitable" regime above. These results suggest that the hypergolic ignition occurs when the size ratio is sufficiently small, and that increasing the Weber number augments the critical size ratio.

The effects of the size ratio on the hypergolic ignitability can be understood from two aspects. From the physical aspect, increasing the size ratio enhances the droplet mixing and hence the exothermic liquid-phase reaction, which is crucial for droplet heating, vaporization and decomposition of the propellants. From the chemical aspect, increasing the size ratio cubically deviates from the chemical stoichiometry of the liquid-phase reaction, TMEDA + 2NA → TMEDADN, because the WFNA droplet size is fixed in the present study and a larger size ratio means a smaller TMEDA droplet. The dominant chemical effect of the size ratio over its physical effect results in the favor of the hypergolic ignition to smaller size ratios. For the ignitable cases, the ignition delay times tend to increase with Δ. The appearance of the plateaus of IDTs, as the result of the competition of droplet mixing and chemical stoichiometry, consolidates the above explanation.

Increasing We often tends to enhance the droplet mixing and hence the liquid-phase reaction heat release, yielding a larger critical size ratio for the hypergolic ignitability. By the same token, the ignition delay times tend to decrease with increasing We. A seemingly counterintuitive result has been obtained in the present study that, in a certain (relying on Δ) range of We, the ignition delay times increase with We. This result can be speculatively attributed to the recently identified phenomena in droplet coalescence and internal mixing: the jet-like mixing patterns emerge at relatively small and large Wes but disappear at intermediate Wes. Future studies are merited to seek direct evidence to the speculation.

It is noted that all the above discussions are based on the situation where the WFNA droplet is larger than the TMEDA droplet. It merits a separate, future study to explore the hypergolic ignitability for the cases of $\Delta < 1$, namely, the WFNA droplet is smaller than the TMEDA droplet. For advocating such a study, we have conducted three exploratory experiments, at We = 30.1 and Δ = 0.5, We = 80.3 and Δ = 0.5, We = 30.1 and Δ = 0.7, in which the size of the WFNA droplet is fixed at 0.3mm. No ignition was observed for all the three cases. A possible explanation is that these droplets are too small to generate sufficient heat release through the liquid-phase reaction, and additionally the large surface-volume ratios increase the heat loss to the environment.

In the present study, the Ohnesorge number is fixed so that the effects of liquid viscosity remain to be characterized. The thermal effect of the viscous dissipation on the hypergolic ignition delay is unlikely to be significant compared with the chemical heat release from the liquid-phase reaction of TMEDA and HNO_3. The fluid-dynamic influence of viscosity on the droplet separation and in turn the hypergolic ignition may be of interest and merits future study. Independent variation of Oh in the present problem can be only realized by varying D_O because the physical properties of WFNA are fixed. Adopting larger droplets in the experiment may cause the asphericity of droplets while adopting smaller droplets would signify the additional physics of heat loss in the present problem.

The above considerations urge a future study on the comprehensive characterization of the viscosity and size effects. Future efforts can be also made to enclose the experimental apparatus in a pure nitrogen environment with variable pressures to mimic the real engine conditions without atmospheric oxygen.

Acknowledgement

The authors are grateful to Mr. Bing Wang of the Hong Kong Polytechnic University for the technical assistances in the droplet collision apparatus, to Professors Xuejun Fan and Xilong Yu of Institute of Mechanics, Chinese Academy of Sciences, for helping in acquiring high-

speed camera and photoelectric detectors. This work was supported by the Hong Kong RGC/GRF (PolyU 152217/14E) and partially by the Central Research Grants of the Hong Kong Polytechnic University (operating under contract number G-UA2M and G-YBGA).

Reference

[1] G.P. Sutton, O. Biblarz, Rocket propulsion elements, 8ed., John Wiley & Sons, Hoboken, New Jersey, 2010.

[2] E.A. Fletcher, G. Morrell, Ignition in liquid propellant rocket engines, in: M.G. J. Ducerme, A. H. Lefebvre (Ed.), Progress in Combustion Science and Technology Volume I, Pergamon, Oxford. London. New York. Paris, 1960, pp. 183-215.

[3]] R.J.M. Eric A. Hurlbert, Propellant Ignition and Flame Propagation, in: V. Yang, M. Habiballah, J. Hulka, M. Popp (Eds.), Liquid Rocket Thrust Chambers: Aspects of Modeling, Analysis, and Design, American Institute of Aeronautics and Astronautics, Inc., Virginia, 2004.

[4] S.M. Davis, N. Yilmaz, Advances in Hypergolic Propellants: Ignition, Hydrazine, and Hydrogen Peroxide Research, Adv. Aerosp. Eng. 2014 (2014) 1-9.

[5] C.D. McKinney Jr, M. Kilpatrick, An Apparatus for Measuring the Rates of Some Rapid Reactions, Rev. Sci. Instrum. 22 (1951) 590-597.

[6] M. Kilpatrick, L.L. Baker. A Study of Fast Reactions in Fuel-oxidant Systems: Anhydrous Hydrazine with 100 percent Nitric Acid, Symp. (Int.) Combust, (1955) 196-205.

[7] R.L. Schalla, E.A. Pletcher. The Behavior of The System Triethylamine—White Fuming Nitric Acid Under Conditions of Rapid Mixing, Symp. (Int.) Combust, (1957) 911-917.

[8] R.L. Schalla, The Ignition Behavior of Various Amines with White Fuming Nitric Acid, ARS J. 29 (1959) 33-39.

[9] J.D. Dennis, T.L. Pourpoint, S.F. Son, Ignition of Gelled Monomethylhydrazine and Red Fuming Nitric Acid in an Impinging Jet Apparatus, 47th AIAA/ASME/SAE/ASEE Joint Propulsion Conference & Exhibit, Joint Propulsion Conferences, California, 2011.

[10] J.D. Dennis, S.F. Son, T.L. Pourpoint. Critical Ignition Criteria for Monomethylhydrazine and Red Fuming Nitric Acid in an Impinging Jet Apparatus, 48th AIAA/ASME/SAE/ASEE Joint Propulsion Conference & Exhibit, (2012) 4325.

[11] S. Wang, S.T. Thynell, A. Chowdhury, Experimental Study on Hypergolic Interaction Between N, N, N′, N′-tetramethylethylenediamine and Nitric Acid, Energy & Fuels 24 (2010) 5320-5330.

[12] J. Forness, T.L. Pourpoint, S.D. Heister, Experimental Study of Impingement and Reaction of Hypergolic Droplets, 49th AIAA/ASME/SAE/ASEE Joint Propulsion Conference (2013) 3772.

[13] S. Wang, S. Thynell, An Experimental Study on the Hypergolic Interaction Between Monomethylhydrazine and Nitric Acid, Combust. Flame 159 (2012) 438-447.

[14] E.M. Dambach, Y. Solomon, S.D. Heister, T.L. Pourpoint, Investigation into the Hypergolic Ignition Process Initiated by Low Weber Number Collisions, J. Propul. Power 29 (2013) 331-338.

[15] E.M. Dambach, B.A. Rankin, T.L. Pourpoint, S.D. Heister, Temperature Estimations in the Near-Flame Field Resulting from Hypergolic Ignition Using Thin Filament Pyrometry, Combust. Sci. Technol. 184 (2012) 205-223.

[16] D. Erik, C. Kevin, P. Timothée, H. Stephen, Ignition of Advanced Hypergolic Propellants, 46th AIAA/ASME/SAE/ASEE Joint Propulsion Conference & Exhibit, American Institute of Aeronautics and Astronautics, (2010) 6984.

[17] K.Y. Cho, T.L. Pourpoint, S.F. Son, R.P. Lucht, Microexplosion Investigation of Monomethylhydrazine Gelled Droplet with OH Planar Laser-Induced Fluorescence, J. Propul. Power 29 (2013) 1303-1310.
[18] J.D. Dennis, T.D. Kubal, O. Campanella, S.F. Son, T.L. Pourpoint, Rheological Characterization of Monomethylhydrazine Gels, J. Propul. Power 29 (2013) 313-320.
[19] F.A. Williams, Simplified Theory for Ignition Times of Hypergolic Gelled Propellants, J. Propul. Power 25 (2009) 1354-1357.
[20] M. Orme, Experiments on Droplet Collisions, Bounce, Coalescence and Disruption, Prog. Energy Combust. Sci. 23 (1997) 65-79.
[21] G. Brenn, Droplet Collision, in: N. Ashgriz (Ed.), Handbook of Atomization and Sprays: theory and Applications, Springer, 2011, pp. 157-181.
[22] K.-L. Pan, P.-C. Chou, Y.-J. Tseng, Binary Droplet Collision at Gigh Weber Number, Phys. Rev. E 80 (2009) 036301.
[23] J. Qian, C.K. Law, Regimes of coalescence and separation in droplet collision, J. Fluid Mech. 331 (1997) 59-80.
[24] P. Zhang, C.K. Law, An analysis of head-on droplet collision with large deformation in gaseous medium, Phys. Fluids 23 (2011) 042102.
[25] C. Tang, P. Zhang, C.K. Law, Bouncing, coalescence, and separation in head-on collision of unequal-size droplets, Phys. Fluids 24 (2012).
[26] N. Ashgriz, J. Poo, Coalescence and Separation in Binary Collisions of Liquid Drops, J. Fluid Mech. 221 (1990) 183-204.
[27] C. Rabe, J. Malet, F. Feuillebois, Experimental Investigation of Water Droplet Binary Collisions and Description of Outcomes with a Symmetric Weber Number, Phys. Fluids 22 (2010).
[28] Y.J. Jiang, A. Umemura, C.K. Law, An Experimental Investigation on the Collision Behavior of Hydrocarbon Droplets, J. Fluid Mech. 234 (1992) 171-190.
[29] M. Dai, D.P. Schmidt, Numerical simulation of head-on droplet collision: Effect of viscosity on maximum deformation, Phys. Fluids 17 (2005) 041701.
[30] C. Gotaas, P. Havelka, H.A. Jakobsen, H.F. Svendsen, M. Hase, N. Roth, B. Weigand, Effect of viscosity on droplet-droplet collision outcome: Experimental study and numerical comparison, Phys. Fluids 19 (2007) 102106.
[31] K. Willis, M. Orme, Binary droplet collisions in a vacuum environment: an experimental investigation of the role of viscosity, Exp. Fluids 34 (2003) 28-41.
[32] A. Anilkumar, C. Lee, T. Wang, Surface-tension-induced Mixing Following Coalescence of Initially Stationary Drops, Phys. Fluids 3 (1991) 2587-2591.
[33] C.K. Law, Fuel Options for Next-Generation Chemical Propulsion, AIAA J. 50 (2012) 19-36.
[34] D. Liu, P. Zhang, C.K. Law, Y. Guo, Collision Dynamics and Mixing of Unequal-size Droplets, Int. J. Heat and Mass Transfer 57 (2013) 421-428.
[35] K. Sun, P. Zhang, C.K. Law, T. Wang, Collision Dynamics and Internal Mixing of Droplets of Non-Newtonian Liquids, Phys. Rev. Appl. 4 (2015) 054013.
[36] F. Blanchette, T.P. Bigioni, Dynamics of Drop Coalescence at Fluid Interfaces, J. Fluid Mech. 620 (2009) 333-352.

[37] C. Tang, J. Zhao, P. Zhang, C.K. Law, Z. Huang, Dynamics of Internal Jets in the Merging of Two Droplets of Unequal Sizes, J. Fluid Mech., 795 (2016) 671-689.
[38] K. Sun, T. Wang, P. Zhang, C.K. Law, Non-Newtonian flow effects on the coalescence and mixing of initially stationary droplets of shear-thinning fluids, Phys. Rev. E 91 (2015) 023009.
[39] M.J. McQuaid, W.H. Stevenson, D.M. Thompson, Computationally Based Design and Screening of Hypergolic Multiamines, Proceedings for the Army Science Conference, Orlando, Florida, 2004.
[40] M. McQuaid, Notional Hydrazine-Alternative Hypergols: Design Considerations, Computationally-Based Property Determinations, and Acquisition Possibilities, US Army Research Laboratory, 2006.
[41] W.-G. Liu, S. Dasgupta, S.V. Zybin, W.A. Goddard III, First Principles Study of the Ignition Mechanism for Hypergolic Bipropellants: N, N, N′, N′-Tetramethylethylenediamine (TMEDA) and N, N, N′, N′-Tetramethylmethylenediamine (TMMDA) with Nitric Acid, The J. Phys. Chem. A 115 (2011) 5221-5229.
[42] P. Zhang, L.D. Zhang, C.K. Law, Density Functional Theory Study of The Reactions of 2-azido-N,N-dimethylethanamine with Nitric Scid and Nitrogen Dioxide, Combust. Flame 162 (2015) 237-248.
[43] J.F. Driscoll, C.C. Rasmussen, Correlation and Analysis of Blowout Limits of Flames in High-Speed Airflows, J. Propul. Power 21 (2005) 1035-1044.
[44] W.M. Pitts, The Global Equivalence Ratio Concept And the Formation Mechanisms of Carbon Monoxide in Enclosure Fires, Prog. Energy Combust. Sci. 21 (1995) 197-237.

Figure 1. Schematic of experimental methodologies for hypergolic ignition in (a) a piston-driven apparatus with rapid mixing, (b) an impinging jet test, (c) a drop test, (d) a drop contact test, and by (e) binary droplet collision.

Figure 2. Experimental images (adapted from [35]) of the head-on collision of unequal-size water droplets, showing the non-monotonic emergence of jet-like mixing patterns. The size ratio is fixed at 2.5 and the Weber numbers from left to right are 4.7, 8.1 and 28.7, respectively.

Figure 3. Schematic of the experimental apparatus for hypergolic ignition by binary collision of TMEDA and WFNA droplets. (1) WFNA droplet generator, (2) TMEDA droplet generator, (3) Collection tray, (4) Pressurized liquid tank, (5) Gas tank, (6) Pressure regulator, (7) DC power supply, (8) XYZ and angle displacement stage, (9) Function generator, (10) Controlling circuits.

Figure 4. Schematic of experimental setup for visualizing the hypergolic ignition by time-resolved shadowgraph, visible light detection and infrared radiation detection. (1) High speed camera, (2) Light-emitting diode, (3) Photoelectric detector, (4) Infrared radiation detector, (5) Plano-convex lens, (6) Infrared enhanced mirror, (7) Oscilloscope, (8) Pulse generator, (9) Computer.

Figure 5. Grayscale level analysis of the representative shadowgraph images of the hypergolic ignition (a) before droplet collision, (b) before luminous flames appear, and (c) after luminous flames appear.

Figure 6. Shadowgraph images of the hypergolic ignition at selected times for a representative case with We=60.9 and Δ=1.6. t_{inertia} =1.19ms.

Figure 7. Nonflammable condensed-phase products from the representative case shown in Figure 6.

Figure 8. Grayscale level analysis of r_d and r_b for the representative case shown in Figure 6, (a) during the entire process, and (b) around the ignition.

Figure 9. Voltage signals denoting the intensities of visible lights and infrared radiations (a) during the entire process and (b) around the ignition for the presentative case shown in Figure 6.

Figure 10. Ignitability regime nomogram in the We-Δ subspace of We = 20~220 and Δ = 1.2~2.9.

Figure 11. Shadowgraph images of the hypergolic ignition by collisions with a fixed Δ = 1.6, (a) We = 37.0, $t_{inertia}$ = 1.5ms, (b) We = 52.0, $t_{inertia}$ = 1.3ms, (c) We = 70.8, $t_{inertia}$ = 1.1ms, and (d) We = 83.0, $t_{inertia}$ = 1.0ms.

Figure 12. Dependence of ignition delay times on the Weber number at various droplet size ratios of 1.3, 1.6 and 2.2.

Figure 13. Shadowgraph images of the hypergolic ignition by collisions with a fixed We = 60.9 and (a) Δ = 1.2, (b) Δ = 2.2, and (c) Δ = 2.8. $t_{inertia}$ = 1.2ms for (a), (b) and (c).

Figure 14. Dependence of the ignition delay times on the size ratio at the Weber numbers of 60.9 ($t_{inertia}$=1.2ms) and 83.0 ($t_{inertia}$=1.0ms).

figure 1.jpg
Click here to download high resolution image

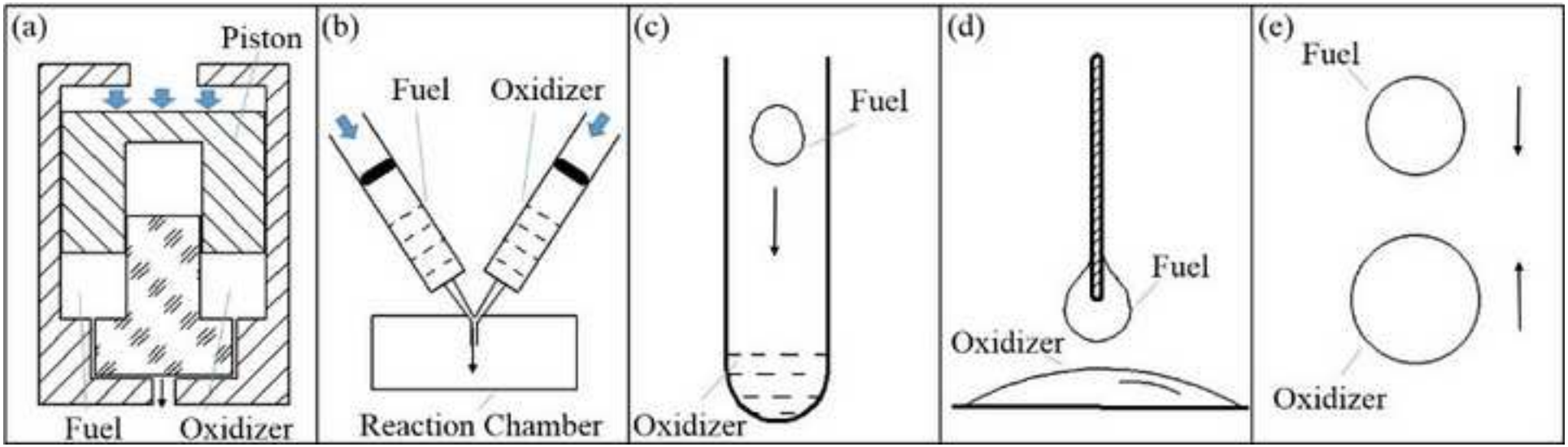

figure 10.tif
Click here to download high resolution image

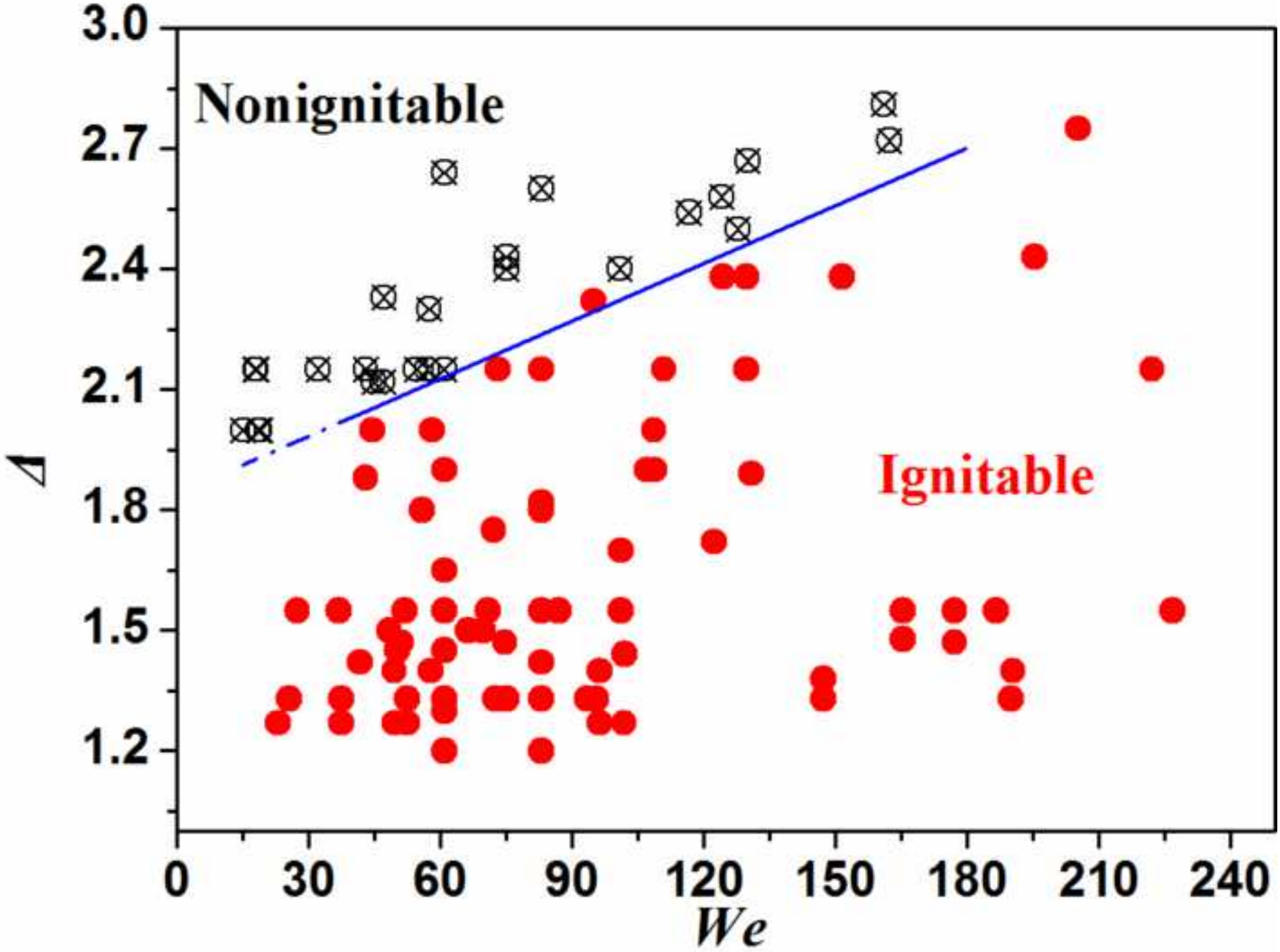

figure 11a.jpg
Click here to download high resolution image

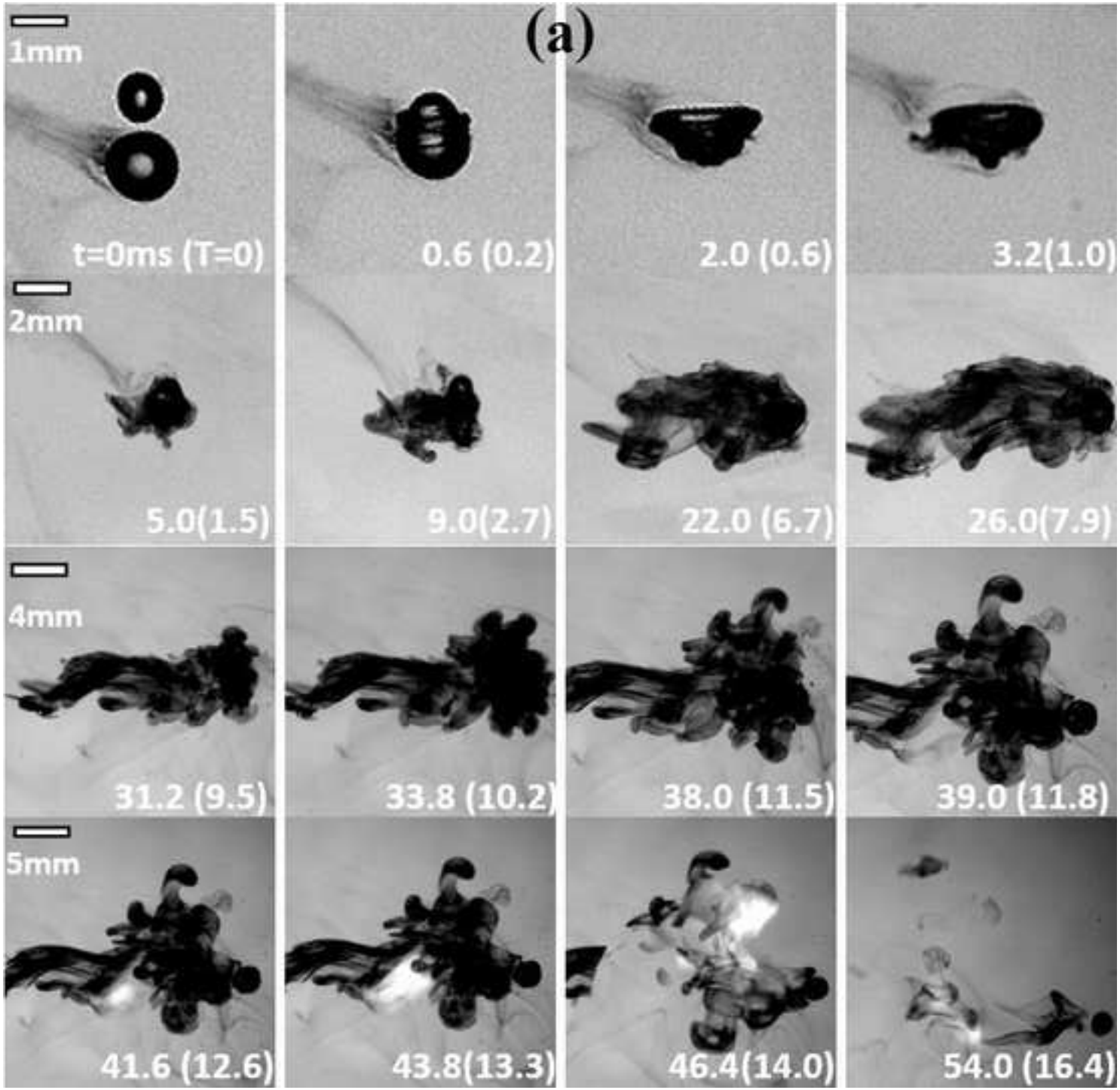

figure 11b.jpg
Click here to download high resolution image

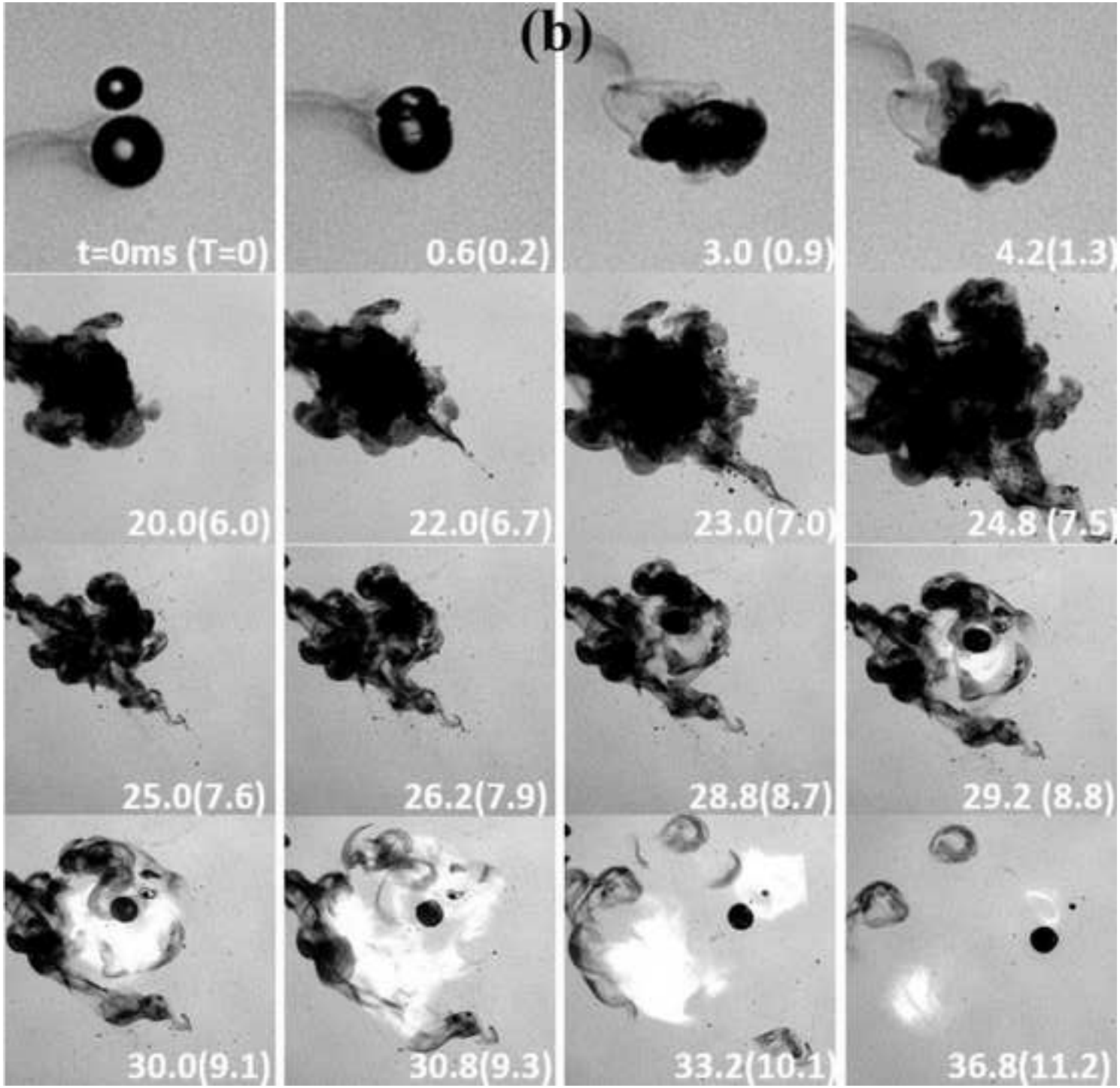

figure 11c.jpg
Click here to download high resolution image

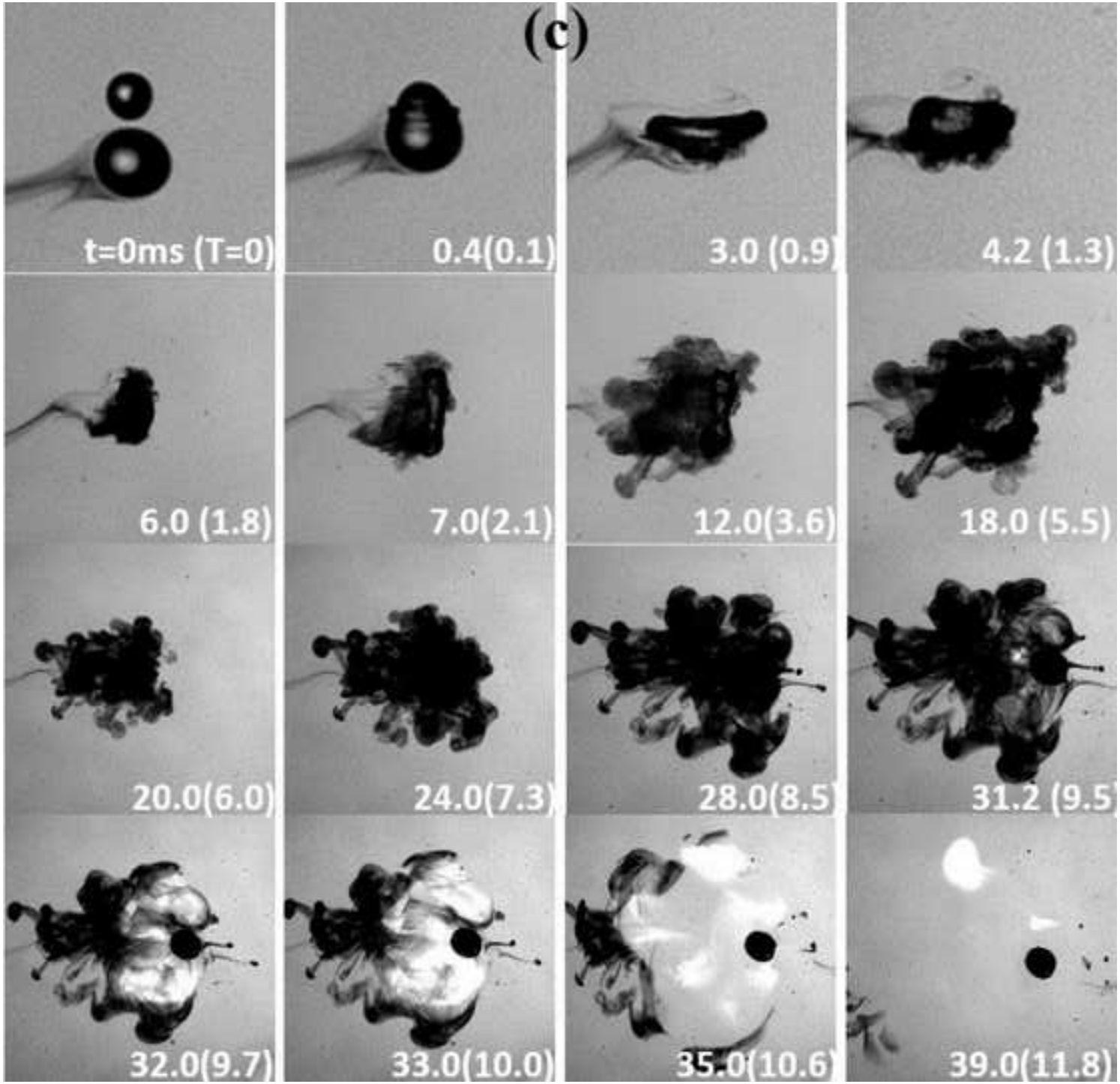

figure 11d.jpg
Click here to download high resolution image

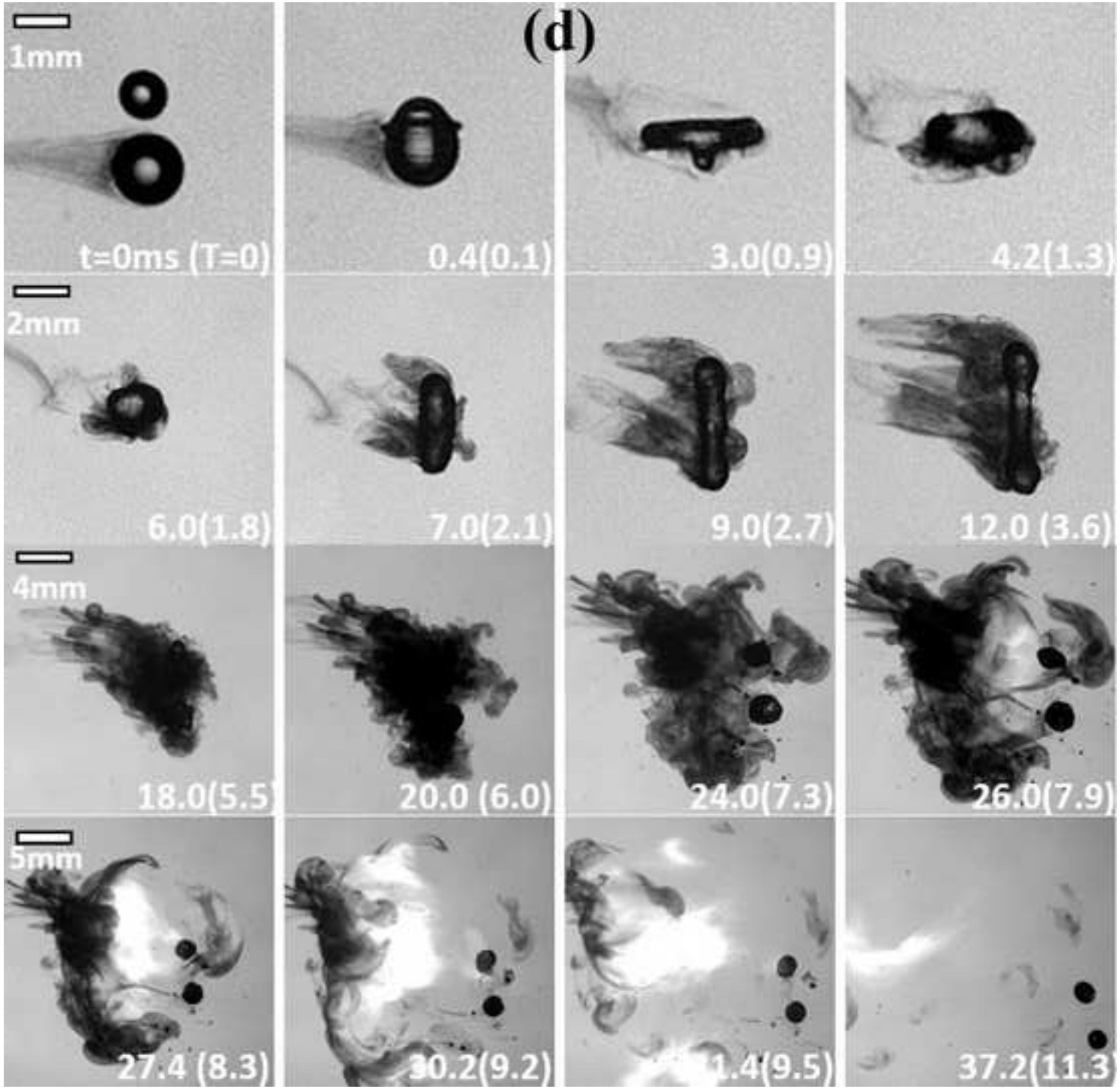

figure 12.tif
Click here to download high resolution image

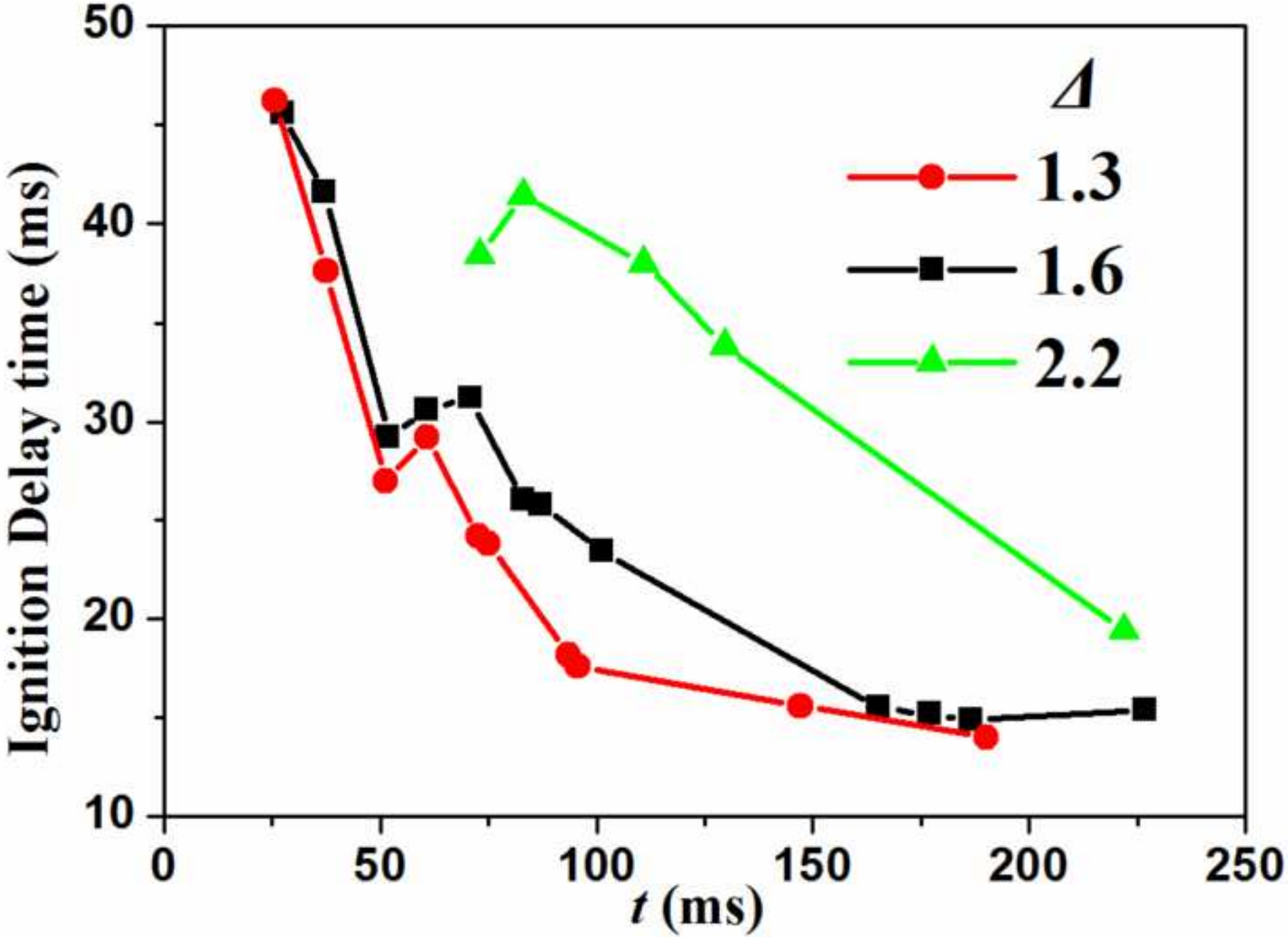

figure 13a.jpg
Click here to download high resolution image

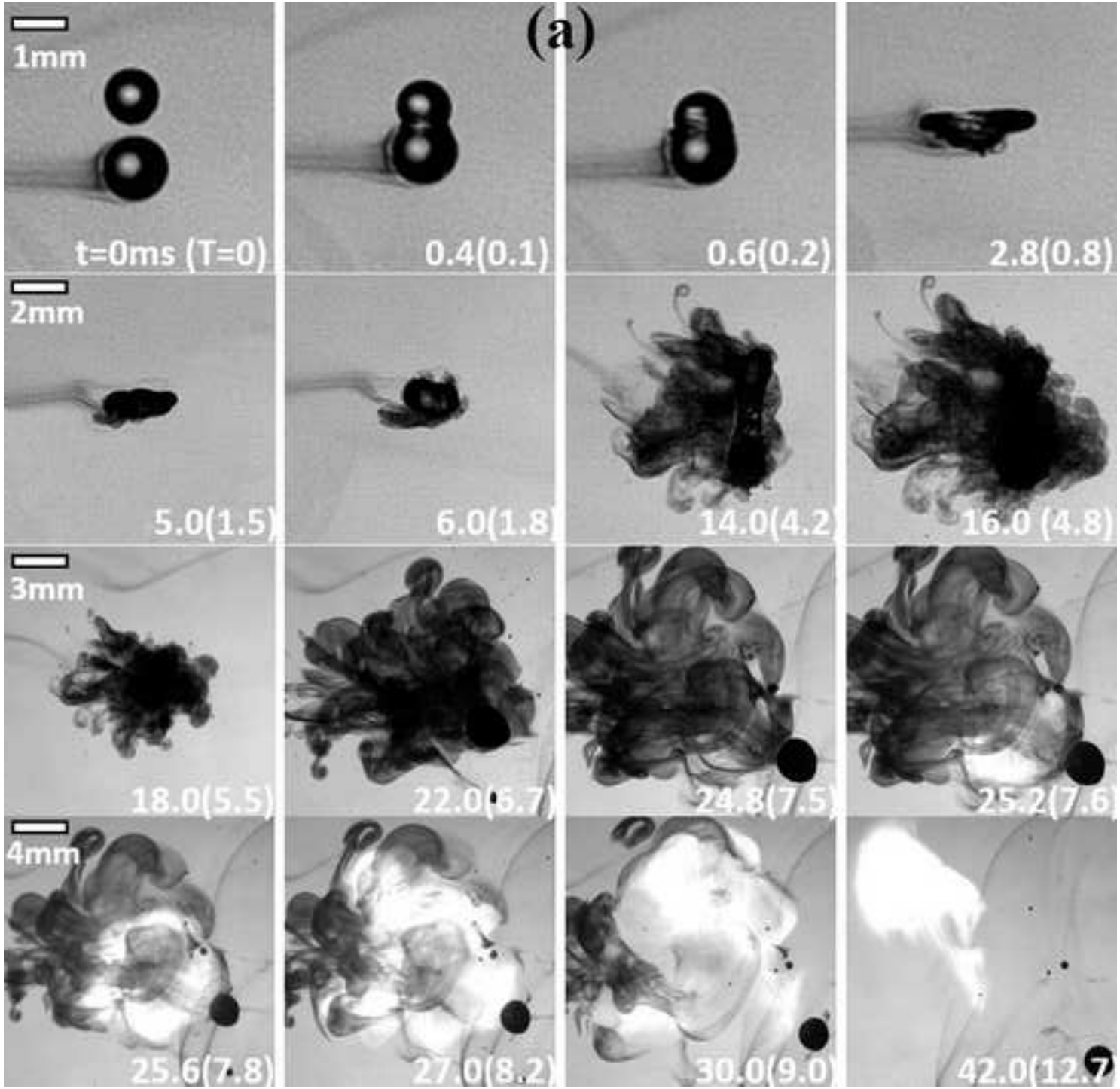

figure 13b.jpg
Click here to download high resolution image

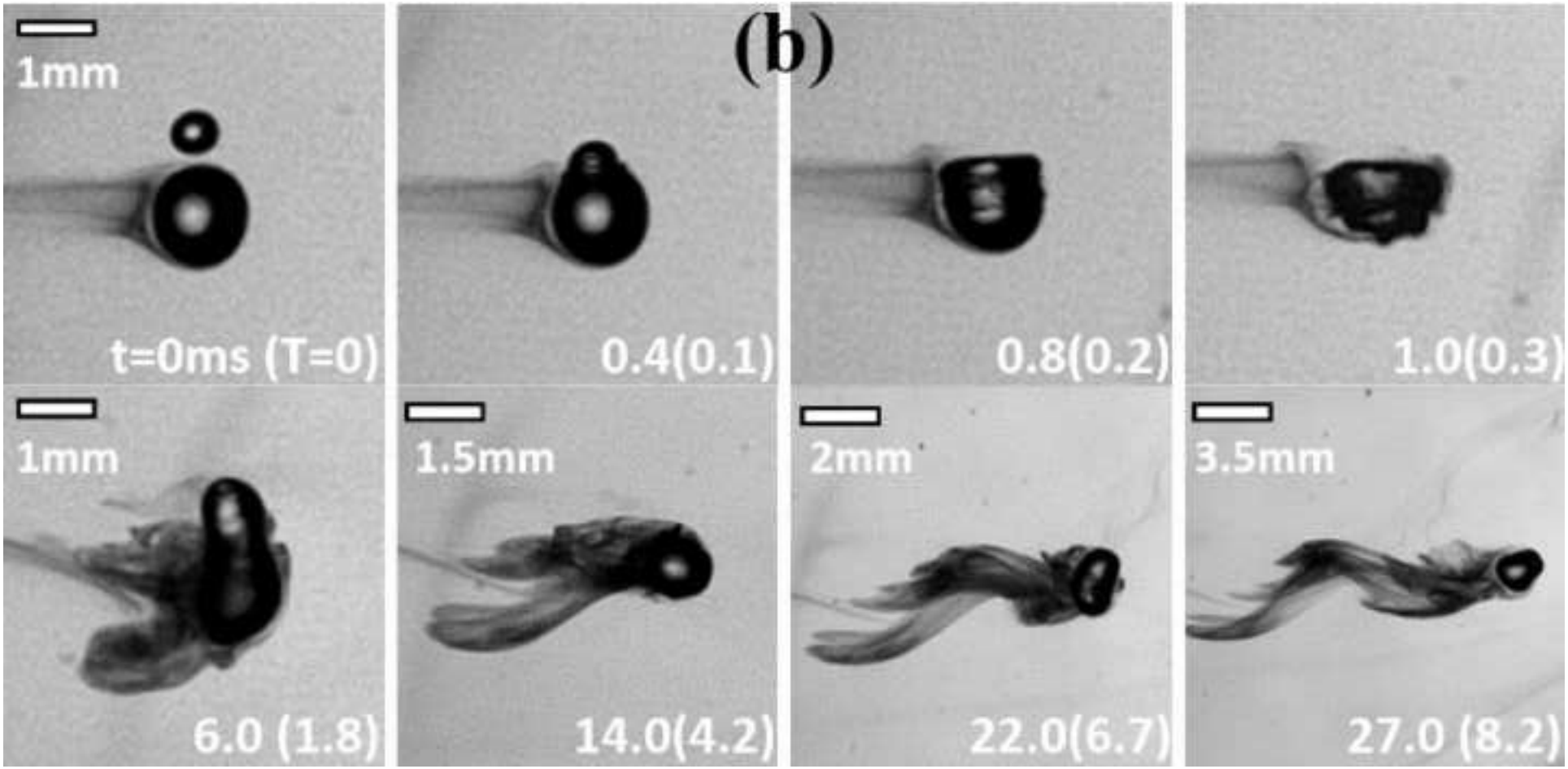

figure 13c.jpg
Click here to download high resolution image

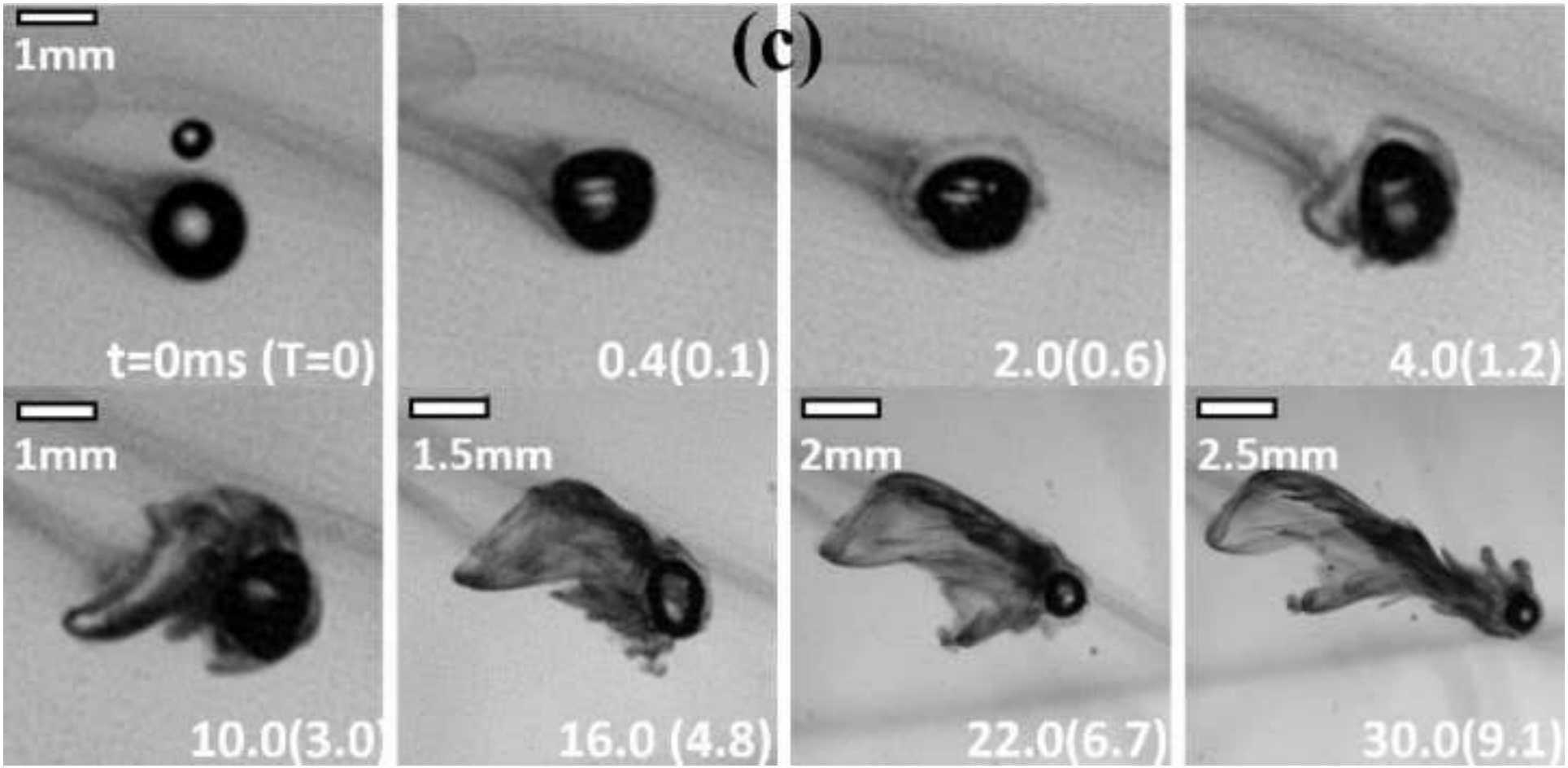

figure 14.tif
Click here to download high resolution image

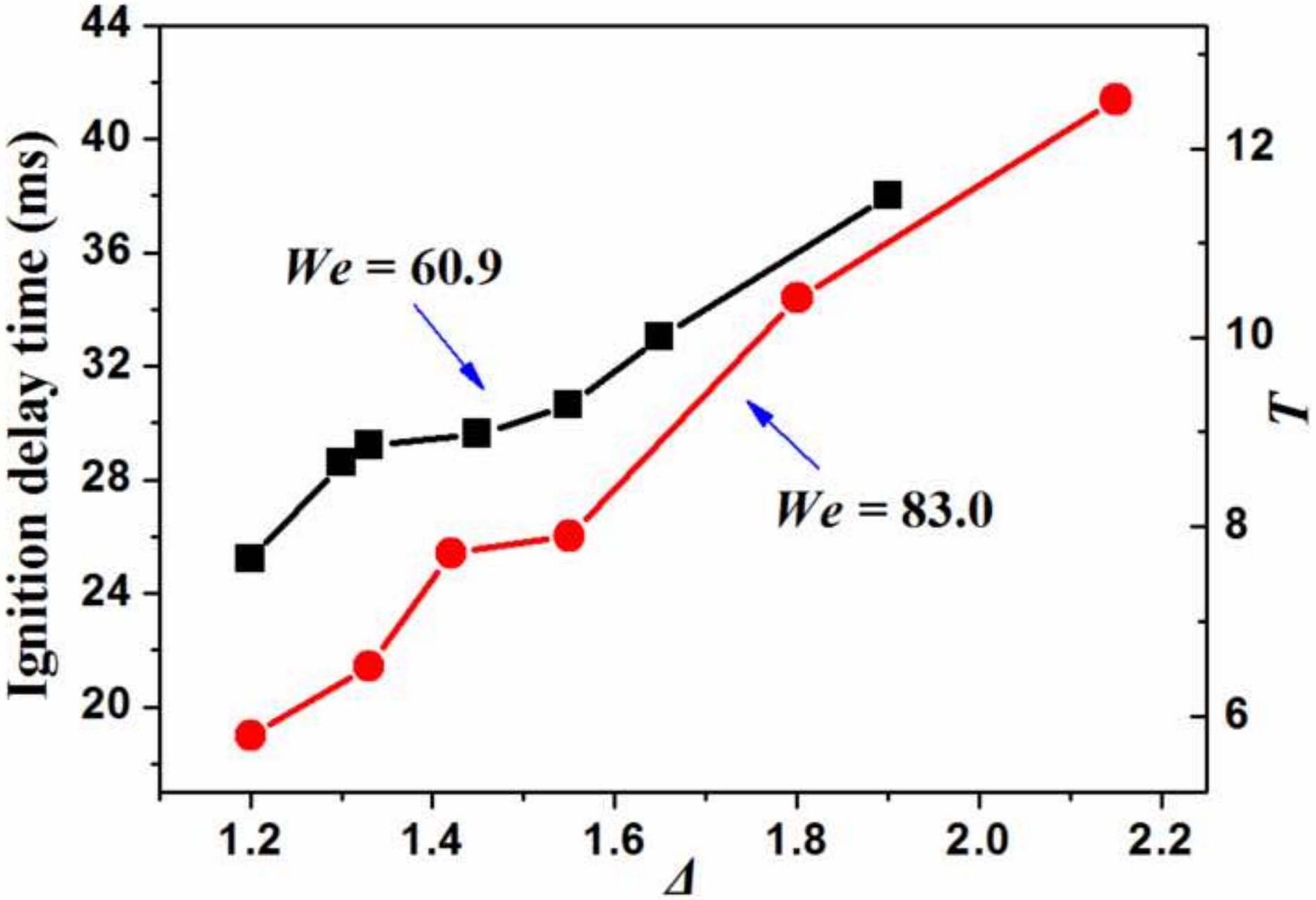

figure 2.jpg
Click here to download high resolution image

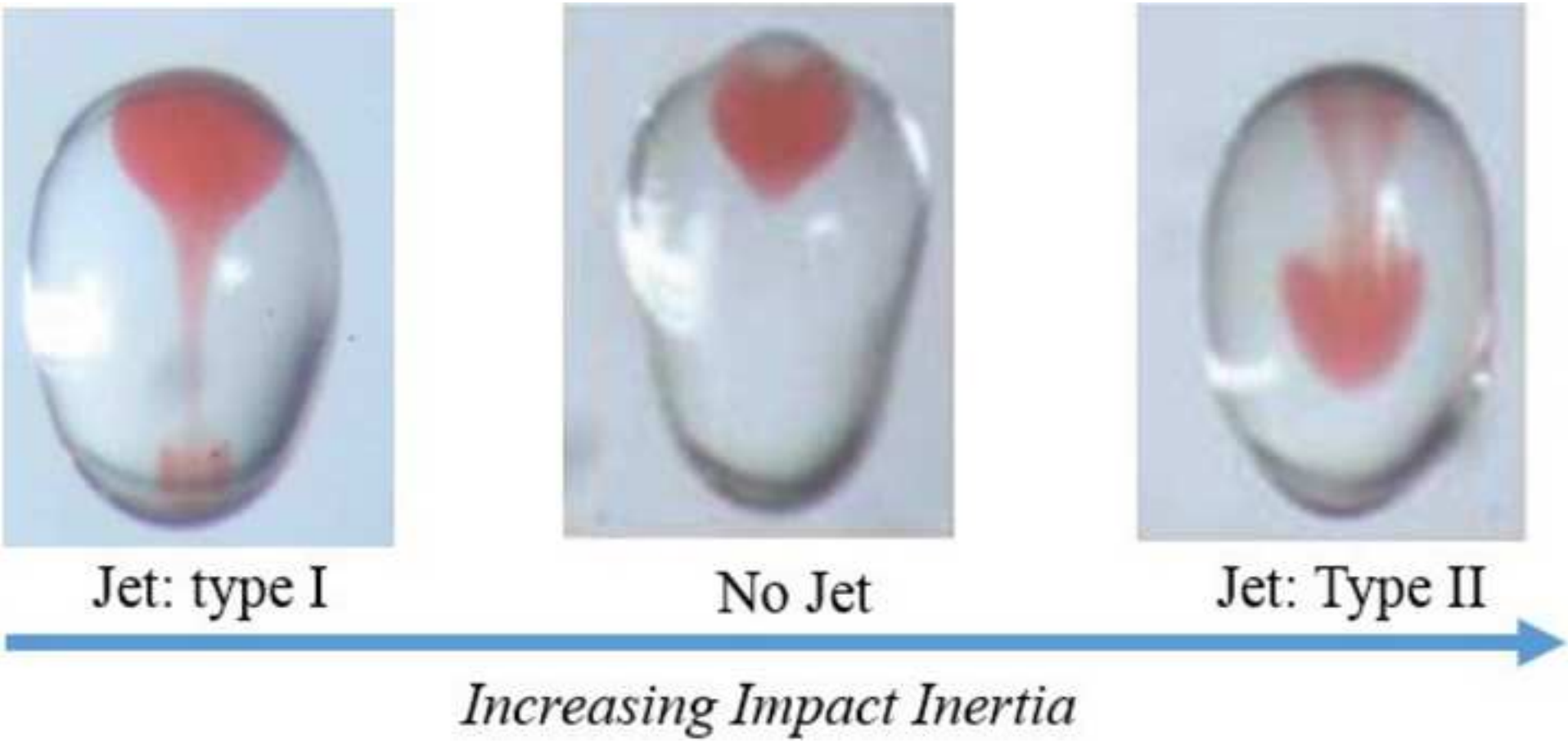

figure 3.jpg
Click here to download high resolution image

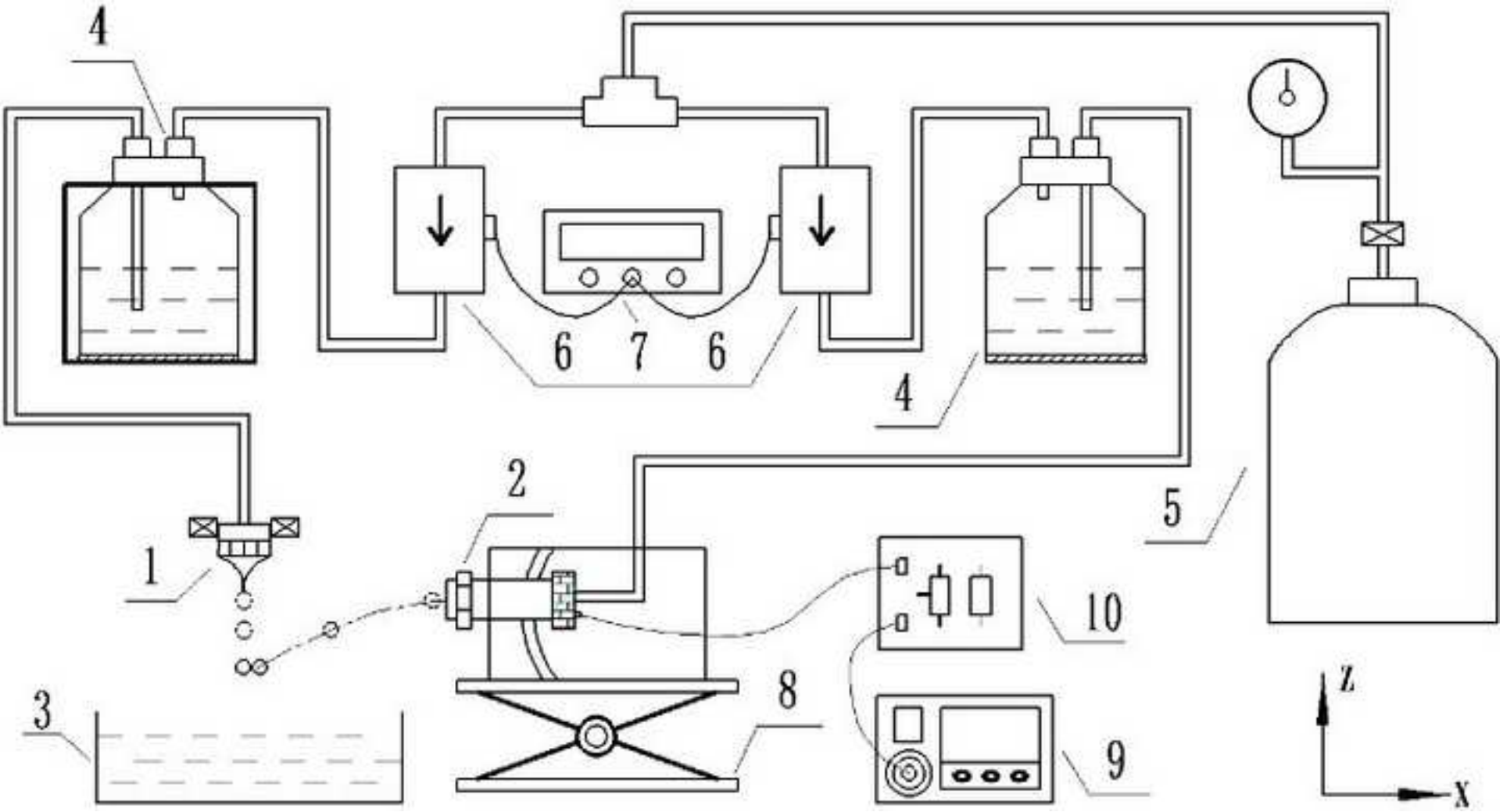

figure 4.jpg
Click here to download high resolution image

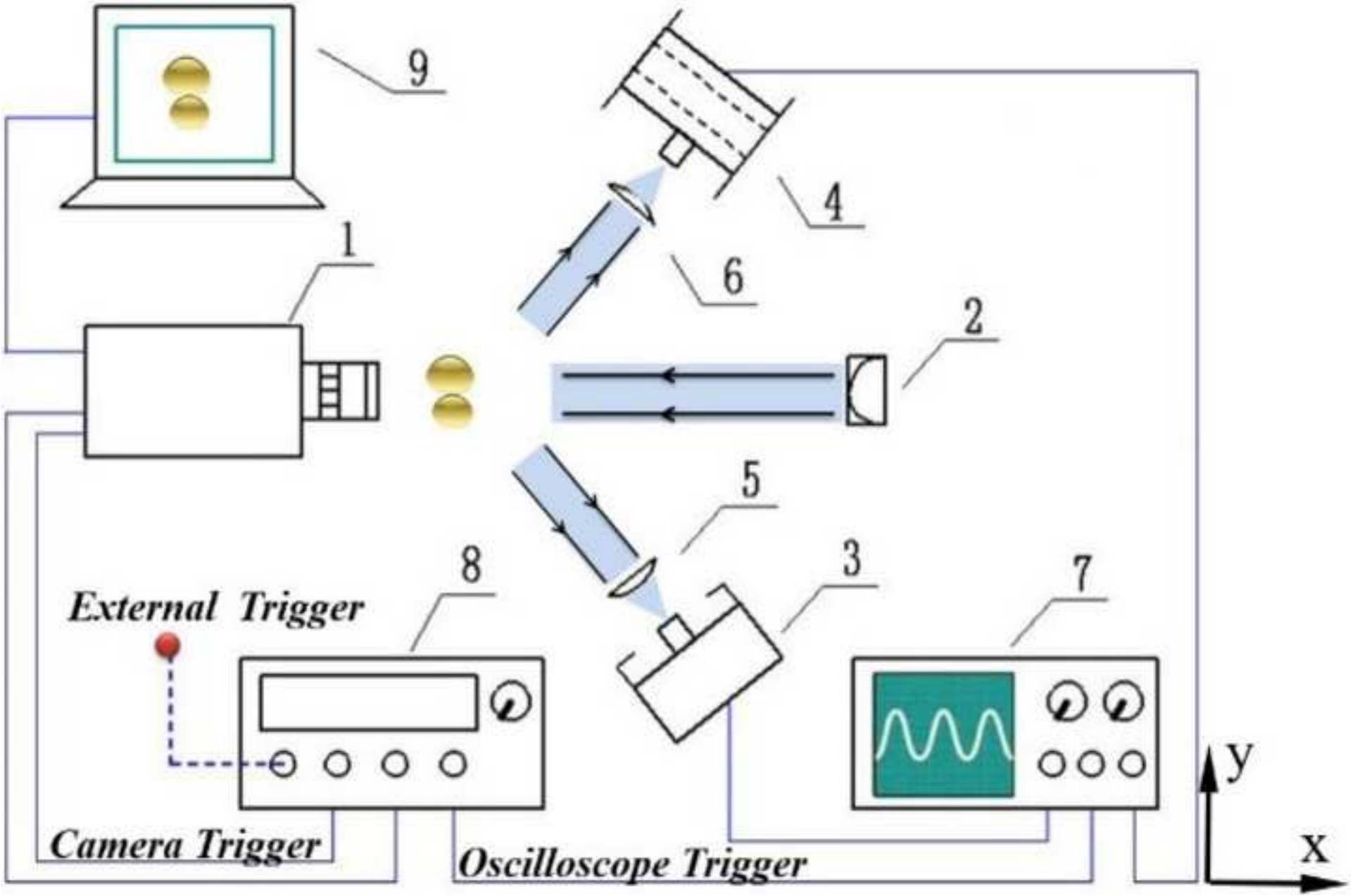

figure 5.jpg
Click here to download high resolution image

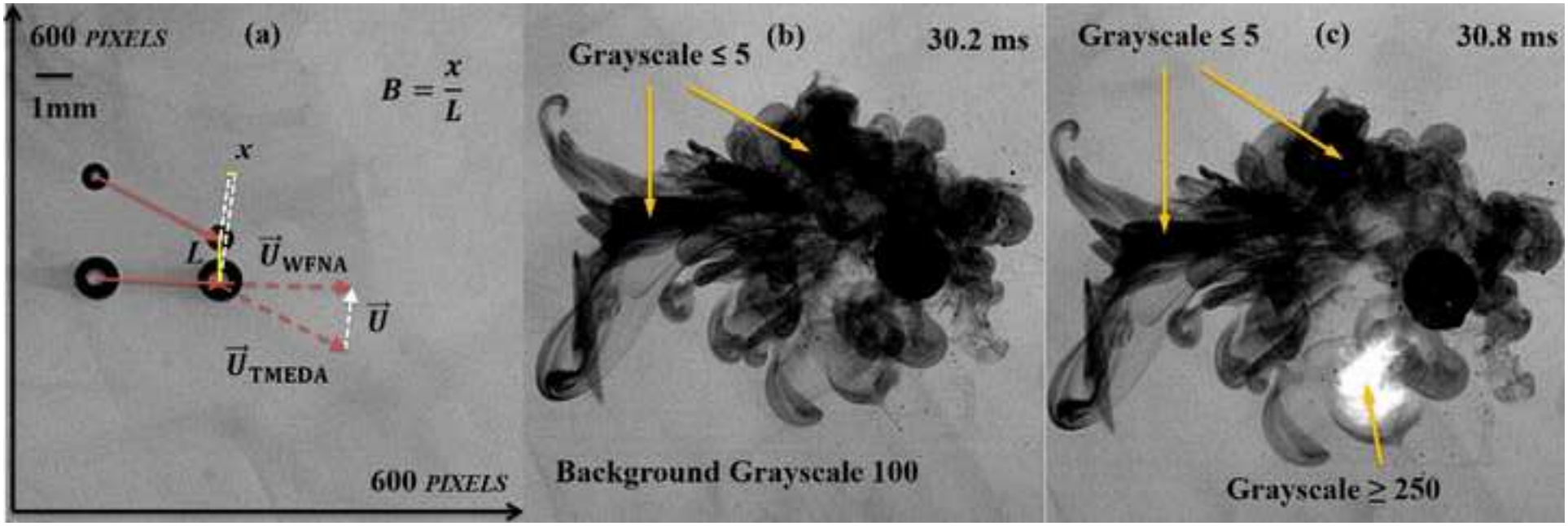

figure 6.jpg
Click here to download high resolution image

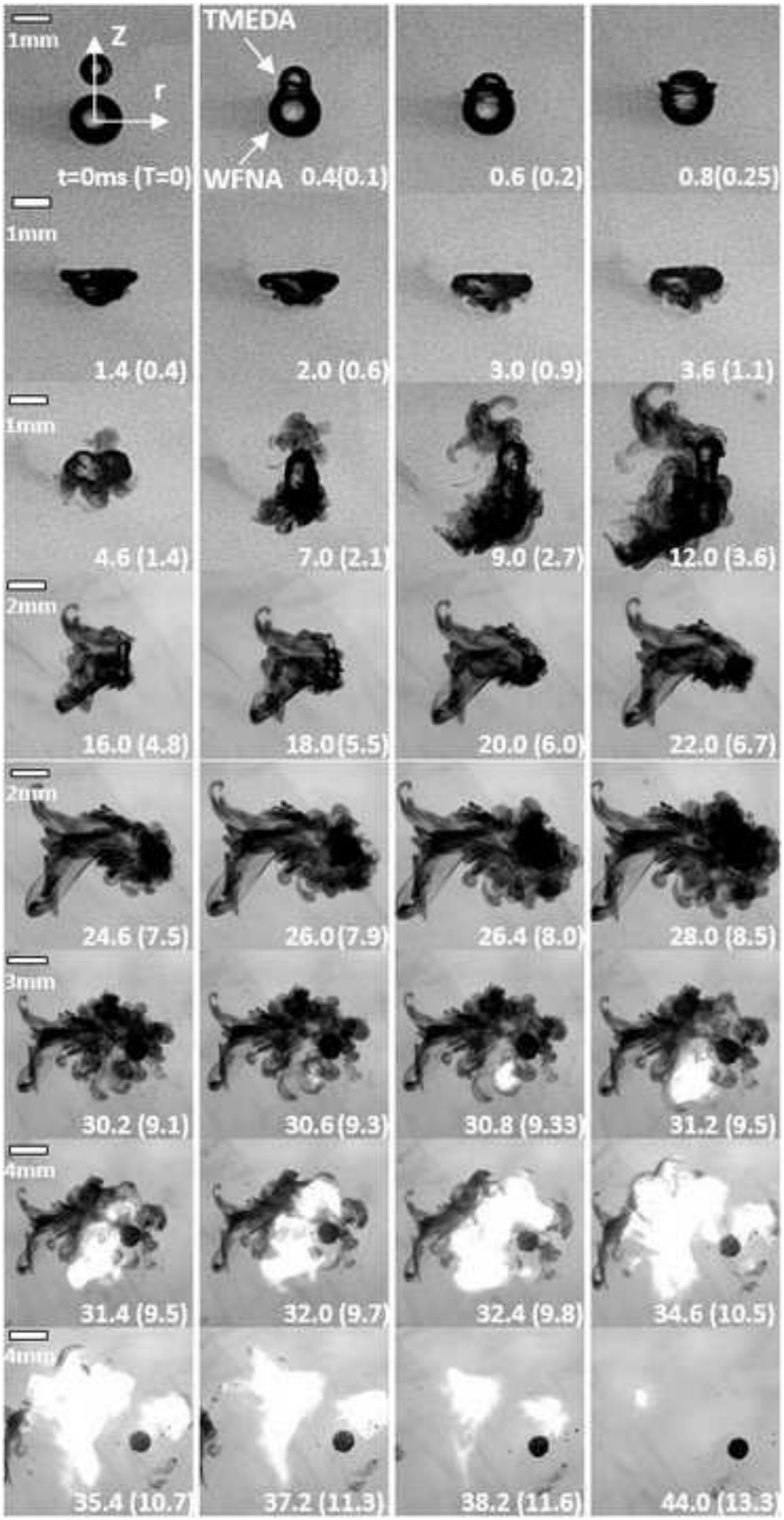

figure 7.jpg
Click here to download high resolution image

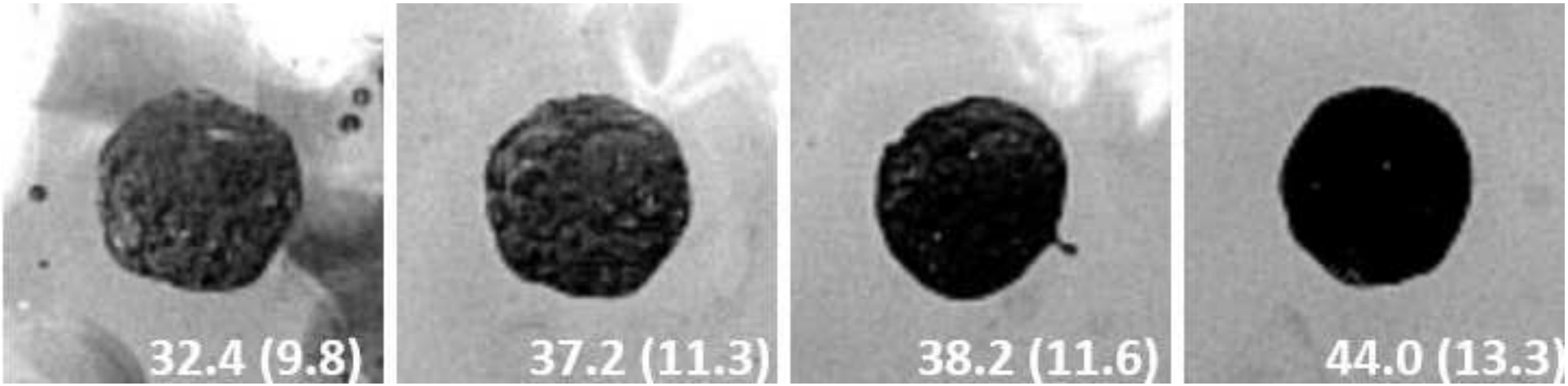

figure 8.tif
Click here to download high resolution image

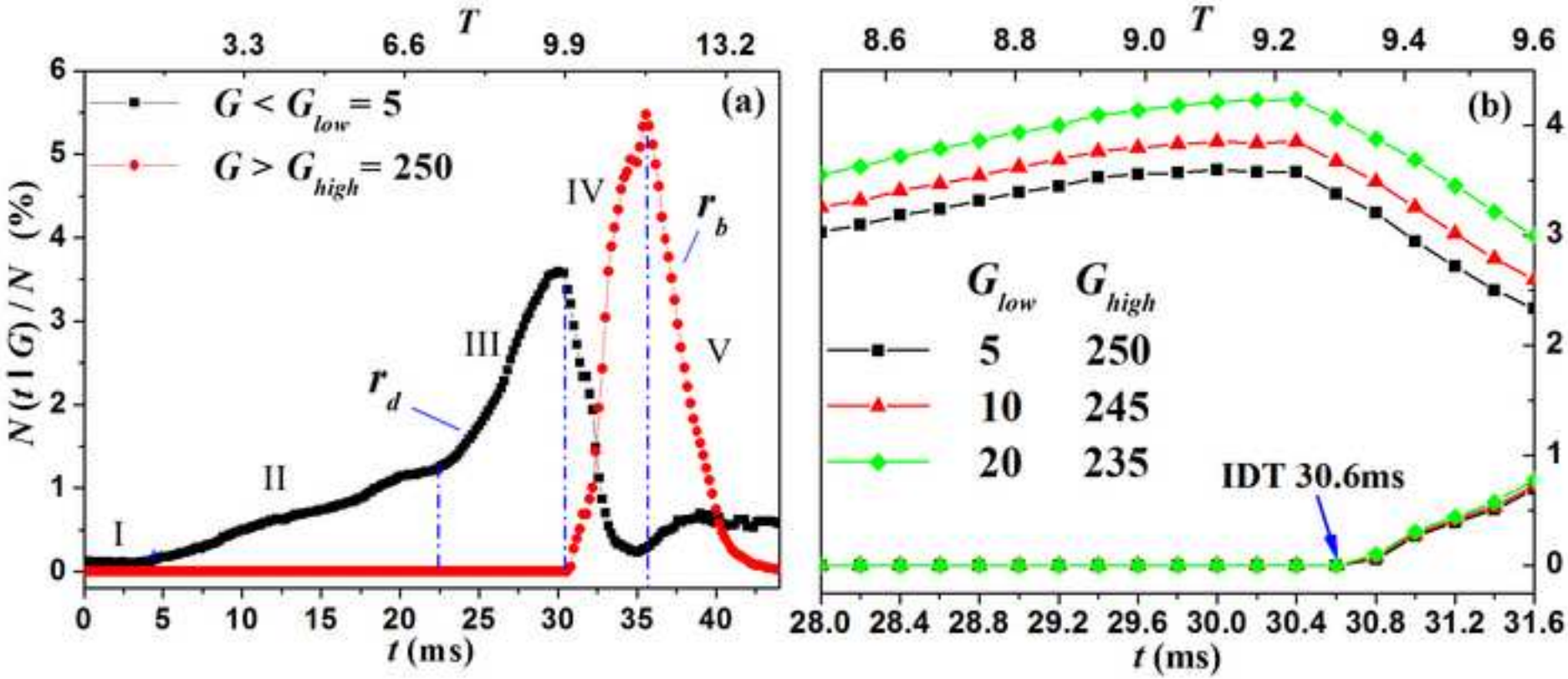

figure 9.tif
Click here to download high resolution image